

Atmospheric parameters and chemical properties of red giants in the CoRoT asteroseismology fields $\star \star \star$

T. Morel¹, A. Miglio^{2,3}, N. Lagarde^{2,3}, J. Montalbán¹, M. Rainer⁴, E. Poretti⁴, P. Eggenberger⁵, S. Hekker^{6,7}, T. Kallinger^{8,9}, B. Mosser¹⁰, M. Valentini^{1,11}, F. Carrier⁸, M. Hareter⁹, and L. Mantegazza⁴

¹ Institut d'Astrophysique et de Géophysique, Université de Liège, Allée du 6 Août, Bât. B5c, 4000 Liège, Belgium

² School of Physics and Astronomy, University of Birmingham, Edgbaston, Birmingham, B15 2TT, UK

³ Stellar Astrophysics Centre (SAC), Department of Physics and Astronomy, Aarhus University, Ny Munkegade 120, DK-8000, Aarhus C, Denmark

⁴ INAF – Osservatorio Astronomico di Brera, via E. Bianchi 46, 23807 Merate (LC), Italy

⁵ Geneva Observatory, University of Geneva, Chemin des Maillettes 51, 1290, Versoix, Switzerland

⁶ Astronomical Institute 'Anton Pannekoek', University of Amsterdam, Science Park 904, 1098 XH Amsterdam, The Netherlands

⁷ Max-Planck-Institut für Sonnensystemforschung, Justus-von-Liebig-Weg 3, 37077 Göttingen, Germany

⁸ Katholieke Universiteit Leuven, Departement Natuurkunde en Sterrenkunde, Instituut voor Sterrenkunde, Celestijnenlaan 200D, B-3001 Leuven, Belgium

⁹ Institute for Astrophysics, University of Vienna, Türkenschanzstrasse 17, 1180 Vienna, Austria

¹⁰ LESIA, CNRS, Université Pierre et Marie Curie, Université Denis Diderot, Observatoire de Paris, 92195 Meudon Cedex, France

¹¹ Leibniz-Institut für Astrophysik Potsdam (AIP), An der Sternwarte 16, 14482, Potsdam, Germany

Received 7 October 2013 / Accepted 19 February 2014

ABSTRACT

A precise characterisation of the red giants in the seismology fields of the CoRoT satellite is a prerequisite for further in-depth seismic modelling. High-resolution FEROS and HARPS spectra were obtained as part of the ground-based follow-up campaigns for 19 targets holding great asteroseismic potential. These data are used to accurately estimate their fundamental parameters and the abundances of 16 chemical species in a self-consistent manner. Some powerful probes of mixing are investigated (the Li and CNO abundances, as well as the carbon isotopic ratio in a few cases). The information provided by the spectroscopic and seismic data is combined to provide more accurate physical parameters and abundances. The stars in our sample follow the general abundance trends as a function of the metallicity observed in stars of the Galactic disk. After an allowance is made for the chemical evolution of the interstellar medium, the observational signature of internal mixing phenomena is revealed through the detection at the stellar surface of the products of the CN cycle. A contamination by NeNa-cycled material in the most massive stars is also discussed. With the asteroseismic constraints, these data will pave the way for a detailed theoretical investigation of the physical processes responsible for the transport of chemical elements in evolved, low- and intermediate-mass stars.

Key words. Asteroseismology – Stars:fundamental parameters – Stars:abundances – Stars:interiors

1. Introduction

Early observations by the MOST (e.g., Kallinger et al. 2008) and WIRE (e.g., Stello et al. 2008) satellites have demonstrated the tremendous potential of extremely precise and quasi-uninterrupted photometric observations from space for studies of red-giant stars. Breakthrough results are currently being made from observations collected by CoRoT (Michel et al. 2008) and *Kepler* (Borucki et al. 2010), which offer the opportunity for the first time to derive some fundamental properties of a vast number of red giants from the modelling of their solar-like oscillations

(see the reviews by Christensen-Dalsgaard 2011, Chaplin & Miglio 2013, and Hekker 2013). Amongst the most exciting results achievable by asteroseismology of red-giant stars are the possibility of inferring their evolutionary status (e.g., Montalbán et al. 2010; Bedding et al. 2011; Mosser et al. 2011), constraining their rotation profile (e.g., Beck et al. 2012; Deheuvels et al. 2012), or determining the detailed properties of the core in He-burning stars (Mosser et al. 2012, Montalbán et al. 2013). In addition, their global seismic properties can provide a high level of accuracy of their fundamental properties, such as masses, radii, and distances, which may then be used to map and date stellar populations in our Galaxy (e.g., Miglio et al. 2009, 2013).

Carrying out an abundance analysis of red-giant pulsators is relevant for two closely related reasons. The most obvious one is that only accurate values of the effective temperature and chemical composition are independently derived from ground-based observations that permit a robust modelling of the seismic data (e.g., Gai et al. 2011; Creevey et al. 2012). Conversely, asteroseismology can provide the fundamental quantities (e.g., mass, evolutionary status) that are needed to best interpret the abundance data. This would allow us, for instance, to better under-

Send offprint requests to: Thierry Morel, e-mail: morel@astro.ulg.ac.be.

* Based on observations collected at La Silla Observatory, ESO (Chile) with the FEROS and HARPS spectrograph at the 2.2 and 3.6-m telescopes under programs LP178.D-0361, LP182.D-0356, and LP185.D-0056.

** Tables A.2 to A.6 are only available in electronic form at the CDS via anonymous ftp to cdsarc.u-strasbg.fr (130.79.128.5) or via http://cdsweb.u-strasbg.fr/cgi-bin/qcat?J/A+A/???/???

stand the physical processes controlling the amount of internal mixing in red giants. One issue of particular interest and is currently actively debated – and this is one of the objectives of this project – is to investigate the nature of the transport phenomena that are known to occur for low-mass stars after the first dredge-up but before the onset of the He-core flash (e.g., Gilroy & Brown 1991).

Thanks to their brightness, a comprehensive study of the chemical properties of the red giants lying in the CoRoT seismology fields is relatively easy to achieve. This can be compared with the case of the fainter stars observed in the exofields of CoRoT (Gazzano et al. 2010; Valentini et al. 2013) or in the *Kepler* field (Bruntt et al. 2011; Thygesen et al. 2012), for which the abundances of the key indicators of mixing (C, N, Li, and $^{12}\text{C}/^{13}\text{C}$) have not been systematically investigated to our knowledge. The most noticeable attempts in the case of the *Kepler* red giants are the low-precision (uncertainties of the order of 0.5 dex) carbon abundances derived for a dozen stars by Thygesen et al. (2012) and the study of lithium in the open cluster NGC 6819 by Anthony-Twarog et al. (2013).

This paper is organised as follows: Sect. 2 presents the targets observed, while Sect. 3 discusses the observations and data reduction. The determination of the seismic gravities is described in Sect. 4. The methodology implemented to derive the chemical abundances and stellar parameters is detailed in Sects. 5 and 6, respectively. The uncertainties and reliability of our results are examined in Sects. 7 and 8, respectively. We present the procedure used to correct the abundances of the mixing indicators from the effect of the chemical evolution of the interstellar medium (ISM) in Sect. 9. Section 10 is devoted to a qualitative discussion of some key results. Finally, some future prospects are mentioned in Sect. 11.

2. The targets

Our sample is made up of 19 red-giant targets for the asteroseismology programme of the satellite. This includes four stars, which were initially considered as potential targets, but were eventually not observed (HD 40726, HD 42911, HD 43023, and HD 175294).¹ The stars lie in either the CoRoT eye pointing roughly towards the Galactic centre (around $\alpha = 18$ h 50 min and $\delta = 0^\circ$) or the anticentre (around $\alpha = 6$ h 50 min and $\delta = 0^\circ$) and were observed during an initial (IR), a short (SR), or a long run (LR) with a typical duration ranging from about 30 to 160 days. The white-light photometric measurements are quasi-uninterrupted (time gaps only occur under normal circumstances during the passage across the South Atlantic Anomaly, resulting in a duty cycle of about 90%).

Three stars based on their radial velocities (HD 170053, HD 170174, and HD 170231) are likely members of the young open cluster NGC 6633. Although membership was also suspected for HD 170031, the radial velocity derived from our ground-based observations is discrepant with the values obtained for the three stars above (Barban et al. 2014; Poretti et al., in preparation) and argues against this possibility unless this star is a runaway (an explanation in terms of binarity can be ruled out). For HD 45398, a possible member of NGC 2232, both our radial velocity and iron abundance are at odds with the values obtained for bona fide members of this metal-rich cluster (Monroe & Pilachowski 2010).

Thanks to seismic constraints, surface gravities are available for all but three of the stars observed by CoRoT. This is dis-

cussed in more detail in Sect. 4. On the other hand, a detailed modelling of the CoRoT data is described for HD 50890 by Baudin et al. (2012) and for HD 181907 by Carrier et al. (2010) and Miglio et al. (2010).

Five bright, well-studied red giants (α Boo, η Ser, ϵ Oph, ξ Hya, and β Aql) with less model-dependent estimates of the effective temperature and surface gravity compared to what can be provided by spectroscopy (from interferometric and seismic data, respectively) were also observed and analysed in exactly the same way as the main targets to validate the procedures implemented.

Relatively inaccurate parallaxes, poorly-known interstellar extinction (many stars lying very close to the plane of the Galaxy)² and unavailability of 2MASS data for the brightest targets conspire to often make the luminosities of the CoRoT targets uncertain. Instead of placing the programme stars in a traditional Hertzsprung-Russell (HR) diagram, we therefore show their position in the $\log T_{\text{eff}}\text{-}\log g$ plane in Fig. 1. Solely based on evolutionary tracks, our sample appears to be made up of stars in various evolutionary stages and that are on average significantly more massive than the Sun. A more complete description of our sample based on asteroseismic diagnostics will be presented in a forthcoming publication (Lagarde et al., in preparation).

3. Observations and data reduction

The scientific rationale of the ESO large programmes devoted to the ground-based observations of the CoRoT targets (LP178.D-0361, LP182.D-0356, and LP185.D-0056; Poretti et al. 2013) has continuously been adapted to the new results obtained by the satellite. The discovery of the solar-like oscillations in red giants (e.g., De Ridder et al. 2009) and their full exploitation as asteroseismic tools (e.g., Miglio et al. 2009, 2013) was one of the most relevant. Therefore, very high signal-to-noise ratio ($S/N \geq 200$) spectra were obtained during the period 2007-2012 to perform an accurate determination of both the stellar parameters (T_{eff} and $\log g$) and the chemical abundances. As a final improvement of the ground-based complement to CoRoT data, dense spectroscopic timeseries were obtained on selected targets (among which HD 45398 and stars in NGC 6633). They are aimed at comparing amplitudes in photometric flux and radial velocity. Double-site, coordinated campaigns involving HARPS and SOPHIE (mounted at the 1.93-m telescope at the Observatoire de Haute Provence, France; OHP) were organised for this purpose (Poretti et al., in preparation).

Most of the observations were obtained with the HARPS spectrograph attached to the 3.6-m telescope at La Silla Observatory (Chile) in either the high-efficiency (EGGS) or the high-resolution (HAM) mode. The spectral range covered is 3780–6910 Å with a resolving power $R \sim 80\,000$ and 115 000, respectively. Spectra of three stars were acquired in 2007 at the ESO 2.2-m telescope with the fiber-fed, cross-dispersed échelle spectrograph FEROS in the object+sky configuration. The spectral range covered is 3600–9200 Å and $R \sim 48\,000$. This wider spectral coverage compared to HARPS allowed a determination of the nitrogen abundance from a few ^{12}CN lines in the range 8002–8004 Å and the $^{12}\text{C}/^{13}\text{C}$ isotopic ratio through the analysis of the ^{13}CN feature at 8004.7 Å.

² Because of the lack of reliable reddening estimates in many cases, no attempts were made to derive the temperatures from colour indices. On the contrary, our spectroscopic results are completely free from these problems.

¹ The CoRoT satellite ceased operations on November 2nd, 2012.

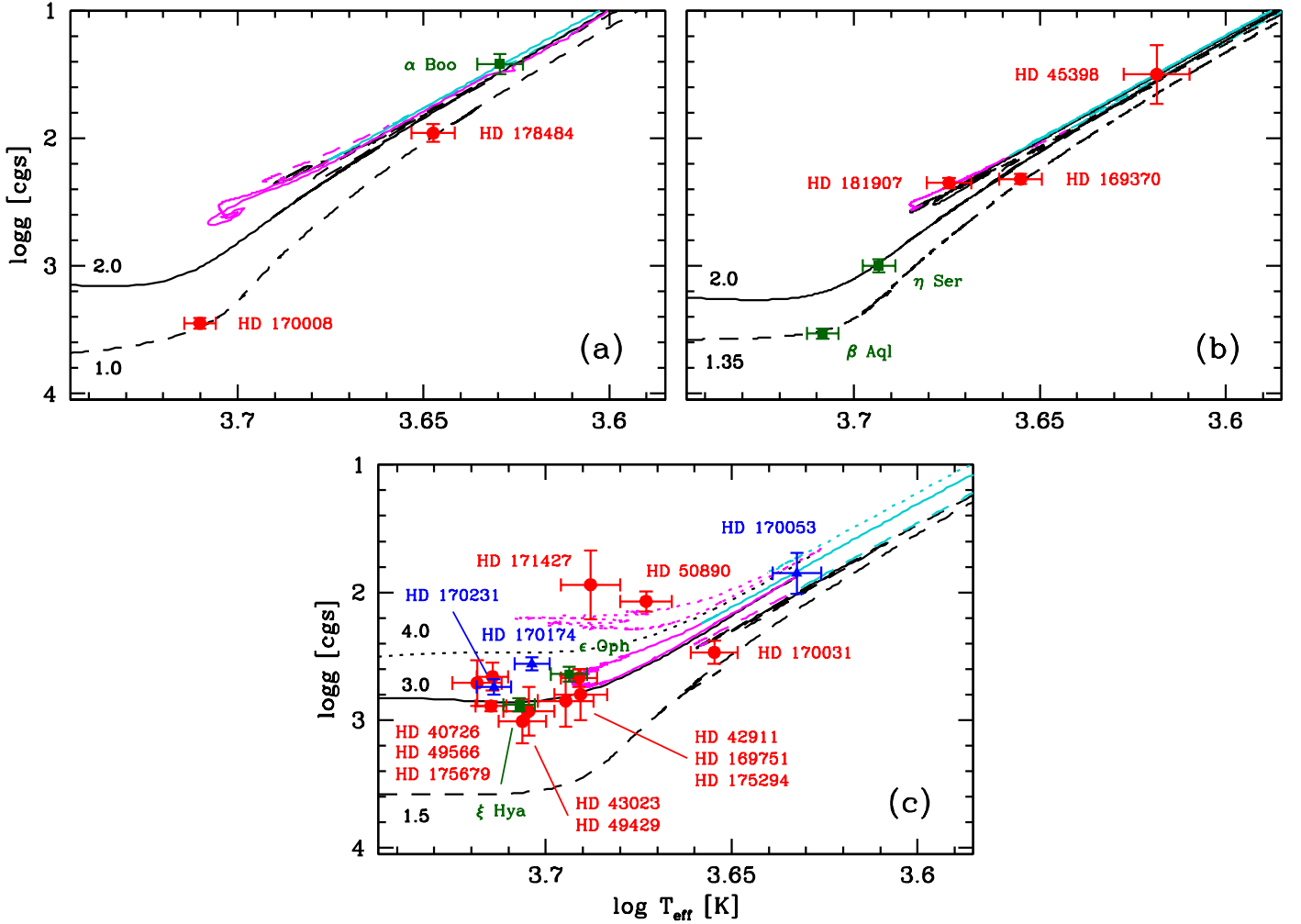


Fig. 1. Position of the targets in the $\log T_{\text{eff}}\text{-}\log g$ plane (red circles: CoRoT targets, blue triangles: stars in NGC 6633, green squares: benchmark stars). The predictions of evolutionary models, which include rotation-induced mixing ($V/V_{\text{crit}} = 0.45$ on the zero-age main sequence; ZAMS) and thermohaline mixing, are overplotted (Lagarde et al. 2012). The initial mass of the models in solar units is indicated to the left of each panel (The tracks are shown with a different linestyle depending on the mass.). The colour of the track indicates the evolutionary phase: red-giant branch (RGB; black), core-He burning (magenta), and asymptotic-giant branch (AGB; cyan). The data are separated into three metallicity domains: theoretical tracks for $[\text{Fe}/\text{H}] = -0.56$ and data for stars with $[\text{Fe}/\text{H}] < -0.26$ (panel a); tracks for $[\text{Fe}/\text{H}] = -0.25$ and data for stars with $-0.26 \leq [\text{Fe}/\text{H}] < -0.12$ (panel b); and tracks at solar metallicity ($Z = 0.014$) and data for stars with $[\text{Fe}/\text{H}] \geq -0.12$ (panel c). When available, the stellar parameters are those obtained with the gravity constrained to the seismic value (Sect. 6).

Four of the bright, benchmark stars were intensively monitored with the ELODIE (ϵ Oph) or the HARPS (η Ser, ξ Hya, and β Aql) spectrographs to study their pulsational behaviour (Further details can be found in De Ridder et al. 2006 and Kjeldsen et al. 2008 for ϵ Oph and β Aql, respectively.). The time series were extracted from the instrument archives. A very high-quality spectral atlas was employed in the case of α Boo (Hinkle et al. 2000). Further details about the observations are provided in Table 1.

The data reduction (i.e., bias subtraction, flat-field correction, removal of scattered light, order extraction, merging of the orders, and wavelength calibration) was carried out for the CoRoT red giants using dedicated tools developed at Brera observatory (Poretti et al. 2013). For the spectra of the benchmark stars extracted from the archives, the final data products provided by the reduction pipelines were used. As a final step, the spectra were put in the laboratory rest frame and the continuum was normalised by fitting low-order cubic spline or Legendre polyno-

mials to the line-free regions using standard tasks implemented in the IRAF³ software. In case of multiple observations, the individual exposures were co-added (weighted by the S/N ratio and ignoring the poor-quality spectra) to create an averaged spectrum, which was subsequently used for the abundance analysis. The only exception was HD 45398, for which we based our analysis on the exposure where [O I] $\lambda 6300$ was the least (in that case negligibly) affected by telluric features.

4. Seismic constraints on the surface gravity

Radii, masses, and surface gravities of solar-like oscillating stars can be estimated from the average seismic parameters that glob-

³ IRAF is distributed by the National Optical Astronomy Observatories, which is operated by the Association of Universities for Research in Astronomy, Inc., under cooperative agreement with the National Science Foundation.

Table 1. Observations and basic parameters of the targets.

HD number	HR number	HIP number	Other Name	Spectral type	Magnitude in the V band	Parallax [mas]	Instrument	Resolving power	Instrumental broadening [Å]	Number of spectra	S/N at 5815 Å
40726	...	28485	...	G5 III	7.00	3.48±0.56	HARPS EGGS	80 000	0.089	1	252
42911	...	29526	...	G7 III	7.38	7.36±0.58	HARPS EGGS	80 000	0.089	1	277
43023	2218	29575	...	G8 III	5.83	10.61±0.38	HARPS EGGS	80 000	0.089	1	342
45398	...	30691	...	K0	6.90	4.58±0.59	HARPS HAM	115 000	0.062	1	249
49429	...	32659	...	K0	6.91	6.19±0.87	HARPS EGGS	80 000	0.089	1	238
49566	...	32705	...	G5	7.71	3.54±0.67	HARPS EGGS	80 000	0.089	1	301
50890	2582	33243	...	G6 III	6.03	2.99±0.44	HARPS EGGS	80 000	0.089	5	396
169370	6892	90238	...	K0	6.30	10.52±0.57	HARPS EGGS	80 000	0.089	1	225
169751	...	90379	...	K2	8.37	7.26±0.75	HARPS EGGS	80 000	0.089	1	200
170008	...	90427	...	G5	7.42	12.45±0.71	HARPS EGGS	80 000	0.089	1	240
170031	K5	8.20	...	HARPS HAM	115 000	0.062	108	141
171427	...	91063	...	K2	7.22	2.06±0.53	HARPS EGGS	80 000	0.089	1	266
175294	...	92807	...	K0	7.40	2.94±0.66	FEROS	48 000	0.151	1	330
175679	7144	92968	...	G8 III	6.14	6.39±0.43	FEROS	48 000	0.151	1	439
178484	...	94053	...	K0	6.61	5.00±0.46	HARPS HAM	115 000	0.062	1	257
181907	7349	95222	...	G8 III	5.82	9.64±0.34	FEROS	48 000	0.151	1	490
170053	K2 II	7.30	2.67±0.32 ^a	HARPS HAM	115 000	0.062	99	154
170174	K2	8.31	2.67±0.32 ^a	HARPS HAM	115 000	0.062	1	158
170231	K2	8.69	2.67±0.32 ^a	HARPS HAM	115 000	0.062	93	137
124897	5340	69673	α Boo, Arcturus	K1.5 III	-0.04	88.83±0.54	KPNO échelle	150 000	0.045	1	~1000 ^b
168723	6869	89962	η Ser	K0 III-IV	3.26	53.93±0.18	HARPS HAM	115 000	0.062	129	246
146791	6075	79882	ϵ Oph	G9.5 III	3.24	30.64±0.20	ELODIE	48 000	0.151	181	184 ^c
100407	4450	56343	ξ Hya	G7 III	3.54	25.16±0.16	HARPS HAM	115 000	0.062	59	284
188512	7602	98036	β Aql, Alshain	G9.5 IV	3.71	73.00±0.20	HARPS HAM	115 000	0.062	135	285

Notes. Spectral types and magnitudes in the V band from SIMBAD database. *Hipparcos* parallaxes from van Leeuwen (2007). The instrumental broadening is the full width at half-maximum of lines measured in calibration lamps at ~ 6700 Å. The quoted S/N is the typical value for one exposure. ^(a) Parallax of the NGC 6633 cluster (van Leeuwen 2009). ^(b) Mean S/N over the wavelength range 3600–9300 Å, as quoted by Hinkle et al. (2000). ^(c) S/N at 5500 Å.

ally characterise their oscillation spectra: the average large frequency separation ($\Delta\nu$) and the frequency corresponding to the maximum oscillation power (ν_{\max}).

Three methods described in Mosser & Appourchaux (2009), Hekker et al. (2010), and Kallinger et al. (2010) were applied to the CoRoT light curves to detect oscillations and measure the global oscillations parameters $\Delta\nu$ and ν_{\max} . We only consider stars for which 2 out of the 3 methods gave a positive detection of both quantities. This was not the case for HD 45398, HD 49429, and HD 171427. The seismic gravities of these three stars are therefore not discussed further. The final values for $\Delta\nu$ and ν_{\max} were adopted from the pipeline developed by Mosser et al. (2010). We determined the uncertainties on $\Delta\nu$ and ν_{\max} by adding the formal uncertainty given by this pipeline and the scatter of the values obtained by the two other methods in quadrature. For HD 170053, the values of $\Delta\nu$ based on the methods of Mosser & Appourchaux (2009) and Hekker et al. (2010) were only considered due to the larger (by a factor ~ 5) uncertainty of the determination provided by the pipeline of Kallinger et al. (2010). For the benchmark stars for which oscillations were detected using sparse/ground-based data, we adopted an uncertainty of 2.5% in $\Delta\nu$ and of 5% in ν_{\max} , as suggested in Bruntt et al. (2010) and also adopted in Morel & Miglio (2012).

The frequency of maximum oscillation power is expected to scale as the acoustic cut-off frequency, and a straightforward relation has been proposed that links ν_{\max} to the surface gravity (e.g., Brown et al. 1991):

$$\log g \simeq \log g_{\odot} + \log \left(\frac{\nu_{\max}}{\nu_{\max, \odot}} \right) + \frac{1}{2} \log \left(\frac{T_{\text{eff}}}{T_{\text{eff}, \odot}} \right). \quad (1)$$

Theoretical support to this scaling law is provided by Belkacem et al. (2011). It is important to stress that this relation is largely insensitive to the effective temperature assumed ($\Delta T_{\text{eff}} = 100$ K leads to $\Delta \log g \sim 0.005$ dex only for a typical red-clump giant.). The average large frequency spacing, on the other hand, scales

approximately as the square root of the mean density of the star (e.g., Tassoul 1980):

$$\Delta\nu \simeq \sqrt{\frac{M/M_{\odot}}{(R/R_{\odot})^3}} \Delta\nu_{\odot}. \quad (2)$$

We have considered several procedures to estimate $\log g$:

- $\log g_0$: using Eq.1 directly and the spectroscopically determined T_{eff} .
- $\log g_1$: using PARAM (da Silva et al. 2006; Miglio et al. 2013), a Bayesian stellar parameter estimation method based on the Girardi et al. (2000) stellar evolutionary tracks, and considering T_{eff} , [Fe/H], $\Delta\nu$, and ν_{\max} as observables.
- $\log g_2$: using PARAM but taking $\Delta\nu$ as the only seismic constraint (see Ozel et al. 2013).
- $\log g_3$: as $\log g_1$ but adopting larger uncertainties in $\Delta\nu$ and ν_{\max} (as suggested in Huber et al. 2013; see below).
- $\log g_4$: as $\log g_2$ but artificially increasing/decreasing the observed $\Delta\nu$ to account for possible biases in Eq. 2 (see below).

When estimating $\log g$, we adopted the following in Eqs. 1 and 2: $\nu_{\max, \odot} = 3090 \mu\text{Hz}$, $\Delta\nu_{\odot} = 135.1 \mu\text{Hz}$ (Huber et al. 2013), and $T_{\text{eff}, \odot} = 5777$ K.

Given that both Eqs.1 and 2 are approximate expressions, we have considered the effect of possible biases in such relations. First, we increased the uncertainties by 2.5% (see also Huber et al. 2013) on both the observed $\Delta\nu$ and ν_{\max} ($\log g_3$). Second, comparisons with stellar models suggest that Eq.2 for stars similar to those in this study is accurate to $\sim 3\%$ (see White et al. 2011; Miglio et al. 2012, 2013, and the analysis presented in Mosser et al. 2013). To check the effect of such a systematic uncertainty on $\log g$, we have increased/decreased the observed $\Delta\nu$ by 2.5%, while we consider it as the only seismic constraint. This led to a couple of gravity values ($\log g_{4a,b}$). The comparison between the different estimates is presented in Fig. 2. As can be seen, there is a good level of consistency between the values

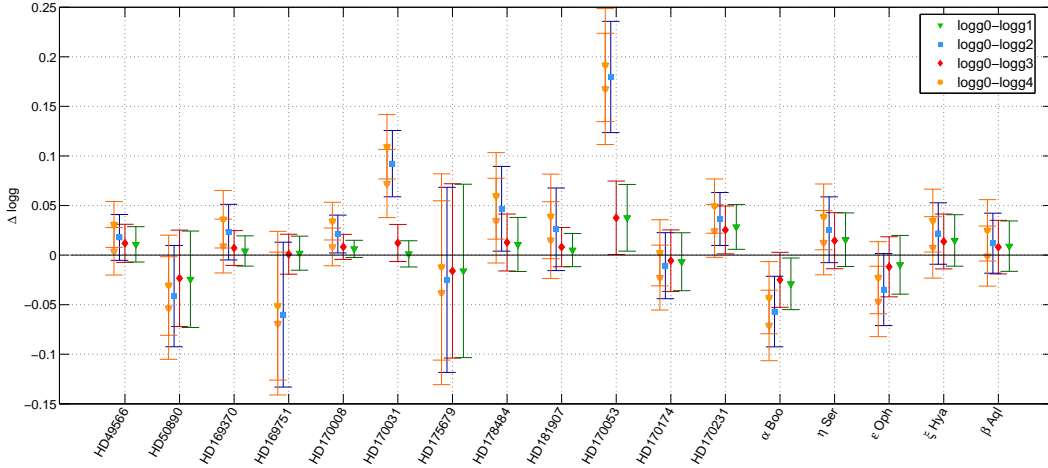


Fig. 2. Comparison of the $\log g$ values determined under different assumptions. The two $\log g_4$ values correspond to an increase/decrease of the observed $\Delta\nu$ by 2.5% (see text).

obtained with the exception of a few cases. The determination of the seismic gravity is therefore robust against the choice of the method used.

However, the difference between $\log g_0$ and $\log g_4$ is particularly prominent for HD 170053, a likely member of the cluster NGC 6633. Using PARAM and all available constraints, we find a stellar mass $M \sim 2.8 M_\odot$, a radius $R \sim 34 R_\odot$, $\log g \sim 1.81$, and $\log(\rho/\rho_\odot) \sim -4.17$. These estimates are compatible with a giant belonging to the cluster, although in a rather fast evolutionary phase (RGB or early AGB). If ν_{\max} is no longer considered as a constraint, then the only strong seismic constraint is on the stellar mean density, and PARAM then finds a low-mass star on the RGB with the values of $M \sim 1.2 M_\odot$, $R \sim 26 R_\odot$, and $\log g \sim 1.67$, which still respects $\log(\rho/\rho_\odot) \sim -4.17$ and the spectroscopic constraints on T_{eff} and $[\text{Fe}/\text{H}]$, as a more likely solution. The turn-off mass of NGC 6633 lies in the range 2.4-2.7 M_\odot (Smiljanic et al. 2009), which excludes the latter possibility if this star is indeed a cluster member.

The final value of $\log g$ we adopted resulted from using Eq. 1 alone ($\log g_0$). Once it was determined, the spectroscopic parameters were re-estimated (Sect. 6), and the procedure was repeated until convergence. The uncertainty was determined as the quadratic sum of the formal uncertainty in $\log g_0$ and the scatter that is between $\log g_0$ and the most discrepant value of the couple $\log g_{4a,b}$ (determined using $\Delta\nu$ only). This leads to the values listed in Table 2.

5. Determination of chemical abundances

The atmospheric parameters (T_{eff} , $\log g$, and microturbulence ξ) and abundances of 12 metals (Fe, Na, Mg, Al, Si, Ca, Sc, Ti, Cr, Co, Ni, and Ba) were self-consistently determined from the spectra using a classical curve-of-growth analysis. On the other hand, the abundances of Li, C, N, and O (as well as the $^{12}\text{C}/^{13}\text{C}$ isotopic ratio for four stars) were determined from spectral synthesis. In each case, Kurucz plane-parallel atmospheric models computed with the ATLAS9 code ported under Linux (Sbordone 2005) and the 2010 version of the line analysis software MOOG originally developed by Sneden (1973) were used. Tests carried out using plane-parallel and spherical MARCS model atmospheres are briefly described in Sect. 7.1. These calculations assume local thermodynamic equilibrium (LTE) and a solar helium abundance. A different atmospheric He content may be encoun-

Table 2. Seismic gravities.

Name	Source of data	$\log g$ seismology [cgs]
HD 45398	CoRoT SRa04	Not available
HD 49429	CoRoT SRa01	Not available
HD 49566	CoRoT SRa01	2.89 ± 0.04
HD 50890	CoRoT IRa01	2.07 ± 0.08
HD 169370	CoRoT LRc03	2.32 ± 0.04
HD 169751	CoRoT LRc03	2.67 ± 0.07
HD 170008	CoRoT LRc03	3.45 ± 0.04
HD 170031	CoRoT LRc07, LRc08	2.47 ± 0.09
HD 171427	CoRoT LRc02	Not available
HD 175679	CoRoT SRc01	2.66 ± 0.11
HD 178484	CoRoT LRc09	1.96 ± 0.07
HD 181907	CoRoT LRc01	2.35 ± 0.04
HD 170053	CoRoT LRc07, LRc08	1.85 ± 0.16
HD 170174	CoRoT LRc07, LRc08	2.56 ± 0.05
HD 170231	CoRoT LRc07, LRc08	2.74 ± 0.06
α Boo	Coriolis satellite	1.42 ± 0.08
η Ser	optical spectra	3.00 ± 0.05
ϵ Oph	MOST satellite	2.64 ± 0.06
ξ Hya	optical spectra	2.88 ± 0.05
β Aql	optical spectra	3.53 ± 0.04

Notes. For the nomenclature of the CoRoT runs, SRa04 is, for instance, the fourth short run in the anticentre direction. Further details about the seismic data for the stars used for validation can be found in Tarrant et al. (2007; α Boo), Barban et al. (2004; η Ser), Kallinger et al. (2008; ϵ Oph), Frandsen et al. (2002; ξ Hya), and Kjeldsen et al. (2008; β Aql). For HD 45398, HD 49429, and HD 171427, the nature of the power spectrum hampered a robust determination of $\Delta\nu$ and/or ν_{\max} . The seismic gravities are therefore not quoted in those cases.

tered within our sample, which is made up of stars in various evolutionary stages, but this is not expected to appreciably affect our results (see Pasquini et al. 2011). Molecular equilibrium was achieved taking into account the 22 most common molecules. As for the solar analysis (see below), all models were computed with a length of the convective cell over the pressure scale height, $\alpha = l/H_p = 1.25$, and without overshooting. Updated opacity distribution functions (ODFs) were employed. They incorporate the solar abundances of Grevesse & Sauval (1998) and a more comprehensive treatment of molecules compared to the ODFs of Kurucz (1990). Further details are provided by Castelli & Kurucz (2004).

5.1. Curve-of-growth analysis

The line list for the 12 metal species ($Z > 8$), whose abundances were directly determined from the equivalent width (EW) measurements, is made up of features selected to be unblended in a high-resolution atlas of the K1.5 III star α Boo (Hinkle et al. 2000). Further details can be found in Morel et al. (2003, 2004). As discussed in these papers, the selected transitions of the odd- Z elements (Sc, Co, and Ba) are not significantly broadened by hyperfine structure. This list was completed by 13 Fe I and 4 Fe II lines taken from Hekker & Meléndez (2007). These lines were carefully chosen to avoid blends with atomic or CN molecular features. Two lines were further added to our list: Na I λ 6160.75 and Al I λ 6696.02.

The EWs were manually measured assuming Gaussian profiles, and only lines with a satisfactory fit were retained. Voigt profiles were used for the few lines with extended damping wings. Atomic lines significantly affected by telluric features were discarded from the analysis (the telluric atlas of Hinkle et al. 2000 was used). The EW measurements are provided in Table A.2.

All the oscillator strengths were calibrated from an inverted solar analysis using a high S/N moonlight FEROS spectrum obtained during our first observing run. The oscillator strengths were tuned until the solar abundances of Grevesse & Sauval (1998) were reproduced. They agree well with the laboratory measurements used by Hekker & Meléndez (2007) with no evidence of systematic discrepancies ($\Delta \log gf = +0.002 \pm 0.100$ dex). Although such a differential analysis with respect to the Sun will not remove the systematic errors inherent to the modelling (e.g., inadequacies in the atmospheric structure) in view of the different fundamental parameters of our targets, such an approach is expected to minimise other sources of systematic errors, such as those related to the data reduction (e.g., continuum placement) or EW measurements. The solar oscillator strengths were derived using a plane-parallel LTE Kurucz solar model⁴ with $T_{\text{eff}} = 5777$ K, $\log g = 4.4377$, and a depth-independent microturbulent velocity, $\xi = 1.0$ km s⁻¹.

Where possible (note that it is the case for the strongest Fe I lines), the damping parameters for the van der Waals interaction were taken from Barklem et al. (2000) and Barklem & Aspelund-Johansson (2005). The long interaction constant, C_6 , was computed from the line broadening cross sections expressed in atomic units, σ , using:

$$C_6 = 6.46 \times 10^{-34} (\sigma/63.65)^{5/2}. \quad (3)$$

A standard dependence of the cross sections on the temperature, as implemented in MOOG, was adopted (Unsöld 1955). As discussed by Barklem et al. (2000), the exact choice of the velocity parameter value, α , does not usually lead to significant differences in the line profile. For lines without detailed calculations (about 35%), we applied an enhancement factor, E_γ , to the classical Unsöld line width parameter. No attempt was made to estimate this quantity on a line-to-line basis, and we assumed a typical value for a given ion. This was based on a comparison between our computed line widths and those assuming the classical van der Waals theory (for Fe and Ni) or a compilation of empirical results in the literature (Chen et al. 2000; Feltzing & Gonzalez 2001; Bensby et al. 2003; Reddy et al. 2003; Thorén et al. 2004), which are based on the fitting of strong lines (for Na, Mg, Al, Si, Sc, and Ti). A value $E_\gamma \sim 1.6$ was adopted for both

⁴ This solar model is available online at: <http://wwwuser.oat.ts.astro.it/castelli/>.

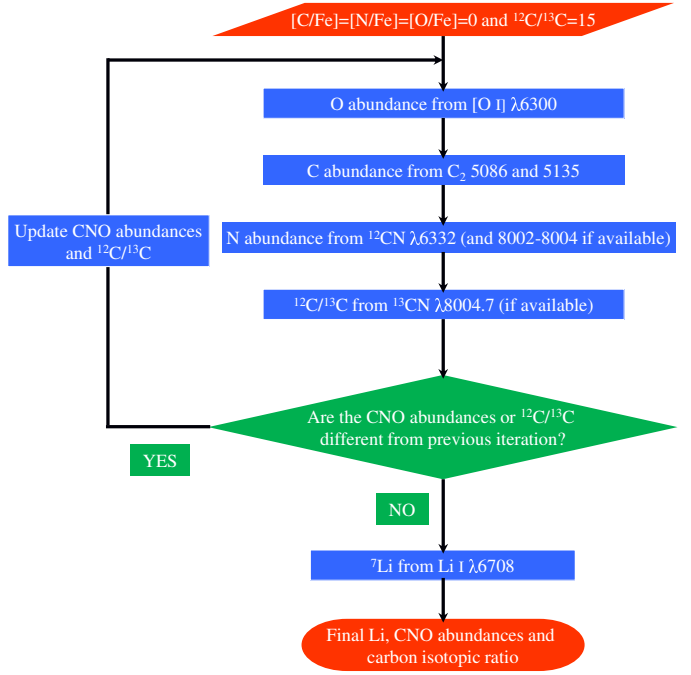


Fig. 4. Iterative scheme used for the spectral syntheses.

the Fe I and Fe II lines. At least for Fe II, the value $E_\gamma = 2.5$ that is often adopted in the literature seems too high (see Barklem & Aspelund-Johansson 2005). A standard treatment of radiative and Stark broadening was used. The line list adopted in our study is provided in Table A.3.

5.2. Spectral synthesis

5.2.1. Line selection and atomic data

The determination of the Li and CNO abundances relied on a spectral synthesis of the following atomic and molecular species: Li I λ 6708 (lithium), the C₂ lines at 5086 and 5135 Å (carbon), ¹²CN λ 6332 (nitrogen), and [O I] λ 6300 (oxygen). For only four stars, a number of ¹²CN lines in the range 8002-8004 Å were also used for nitrogen. Some examples of the fits to the Li and CNO features are shown in the case of HD 175679 in Fig. 3. To ensure molecular equilibrium of the CNO-bearing molecules, the abundances of these three elements were iteratively varied until the values used were eventually the same in each synthesis. The scheme used is sketched in Fig. 4. In all cases, the list of atomic lines of other elements in the spectral ranges of interest was created using the data tabulated in the VALD-2 database assuming the mean abundances based on the EWs. The broadening parameters were estimated as in Sect. 5.1. The linear limb-darkening coefficients in the appropriate photometric band (V , R , or I) were interpolated from the tables of Claret (2000). The following dissociation energies were assumed for the molecular species: $D_0 = 6.21$ (C₂; Huber & Herzberg 1979), 7.65 (CN; Bauschlicher et al. 1988), 6.87 (TiO; Cox 2000), 1.34 (MgH; Cox 2000), and 3.06 eV (SiH; Cox 2000). The effect of adopting other values for C₂ and CN is examined in Sect. 7.2.

The lithium abundance was determined using the accurate laboratory atomic data quoted in Smith et al. (1998). The contribution of the ⁶Li isotope is expected to be negligible and was therefore ignored. The van der Waals damping parameters for the lithium components were taken from Barklem et al. (2000).

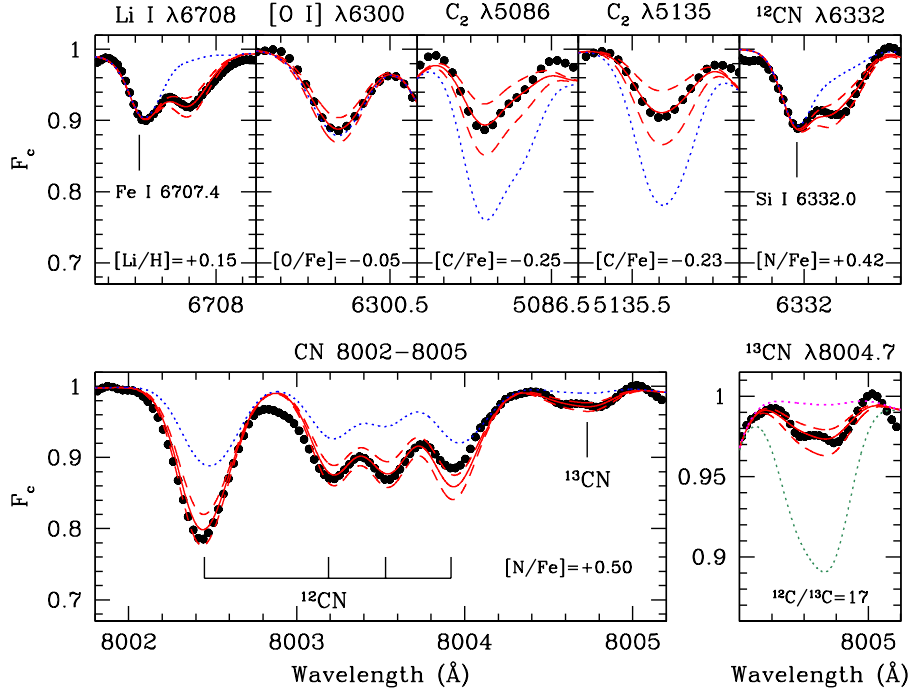


Fig. 3. Example of the fits to the spectral features used as mixing indicators in the case of HD 175679. The solid red line is the best-fitting synthetic profile, while the two dashed lines show the profiles for an abundance deviating by ± 0.1 dex (and deviating by $\Delta^{12}\text{C}/^{13}\text{C} = 5$ in the case of ^{13}CN 8004.7). The blue, dotted lines show the profiles for no Li present (Li I $\lambda 6708$) and solar abundance ratios with respect to iron for the CNO features. In the case of ^{13}CN 8004.7, the magenta and dark green lines show the profiles for $^{12}\text{C}/^{13}\text{C} = 89.4$ and 3.5 , which correspond to the terrestrial and CNO-equilibrium values, respectively.

Spectral features of the diatomic molecules CN, TiO, MgH, and SiH were considered. An extensive CN line list was taken from Mandell et al. (2004), who used a carbon arc spectrum to accurately estimate the wavelengths and oscillator strengths of the ^{12}CN transitions in the spectral region of interest. A list of ^{48}TiO lines from the γ system was taken from Luck (1977). The relevant atomic data were retrieved from the 2006 catalogue version of the TiO database of Plez (1998).⁵ We carried out test calculations for HD 45398 using the updated and more extensive TiO line list implemented in the VALD-3 database, but this led to negligible differences in the Li abundance. It has to be noted that all the transitions considered have accurate laboratory wavenumbers (Davis et al. 1986). A few MgH and SiH lines of significant strength were also taken from the Kurucz atomic database and incorporated.⁶ An isotopic ratio 1.000:0.127:0.139 was assumed for ^{24}MgH : ^{25}MgH : ^{26}MgH (Asplund et al. 2009). The iron and lithium abundances were adjusted until a satisfactory fit of the blend primarily formed by Fe I $\lambda 6707.4$ and the Li doublet was achieved ($\log gf = -2.21$ was adopted for the Fe line based on an inverted solar analysis.). A close agreement was found in all cases between the abundance yielded by this weak iron line and the mean values found with the EWs. A very small velocity shift ($\lesssim 1 \text{ km s}^{-1}$) was occasionally applied to account for an imperfect correction of the stellar radial velocity. Owing to the weakness of the Li I $\lambda 6708$ feature in some objects or its absence thereof, only an upper limit could be determined. A fit of this feature in our solar spectrum yields $\log \epsilon(\text{Li}) = 1.09$, which we take as reference thereafter. We also provide non-LTE (NLTE)

abundances (which we recommend to use) using corrections interpolated from the tables of Lind et al. (2009) in the following. These NLTE corrections are systematically positive and range from $+0.11$ to $+0.36$ dex. For the Sun, it amounts to $+0.04$ dex. It should be noted that abundances lower at the ~ 0.15 dex level at solar metallicity could be expected if the formation of Li I $\lambda 6708$ is modelled using hydrodynamical simulations that take surface convection into account (Collet et al. 2007). However, no correction for granulation effects was applied here because of the unavailability of detailed predictions on a star-to-star basis.

The contribution of Ni I $\lambda 6300.34$ to [O I] $\lambda 6300.30$ was estimated adopting the oscillator strength determined by Johansson et al. (2003) from laboratory measurements: $\log gf = -2.11$. The oscillator strength of the oxygen line, $\log gf = -9.723$, was inferred from an inverted solar analysis, and $E_\gamma = 1.8$ was assumed. The oxygen abundance could also be determined for four stars using the EWs of the O I triplet at about 7774 \AA . The values found systematically appear larger than those yielded by [O I] $\lambda 6300$ with differences ranging from $+0.07$ (HD 175679) to $+0.26$ dex (HD 175294 and α Boo). Such a discrepancy is commonly observed in red giants and likely arises from the different sensitivity to NLTE effects (e.g., Schuler et al. 2006). For this reason, the triplet abundances are not discussed in the following. One should note that our results based on the forbidden line are also immune to the neglect of surface inhomogeneities related to time-dependent convection phenomena (Collet et al. 2007).

The atomic data for the lines of the C_2 Swan system at 5086 and 5135 \AA were taken from Lambert & Ries (1981). In the case of C_2 $\lambda 5135$, however, small adjustments were applied based on a fit of this feature in the Sun. An enhancement factor, $E_\gamma = 2$, was assumed (Asplund et al. 2005). Both lines could be used for all stars but ϵ Oph (C_2 $\lambda 5086$ is affected by a telluric feature), and

⁵ Available online at: <http://www.graal.univ-montp2.fr/hosted/plez/>.

⁶ Available online at: <http://kurucz.harvard.edu/molecules.html>.

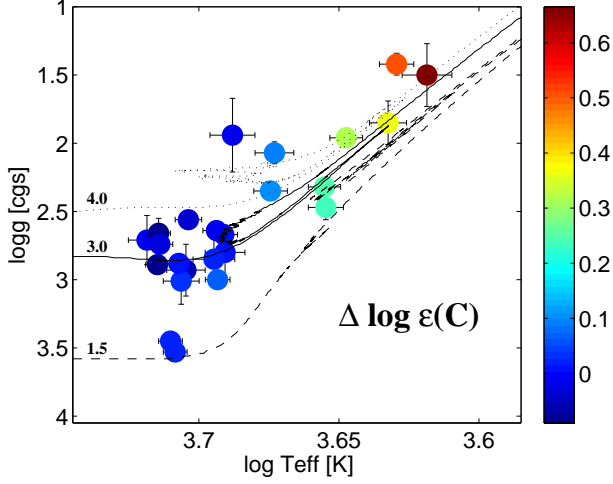


Fig. 5. Difference between the abundances yielded by C₁ λ 5380 and the mean values using the C₂ features. The predictions of evolutionary models at solar metallicity and for masses of 1.5, 3, and 4 M_⊙ are overplotted for illustrative purposes. Same tracks as in Fig. 1, except that the evolutionary phase, is not colour coded.

these two indicators agree closely: $\langle \log \epsilon (\text{C}_2 \lambda 5086) - \log \epsilon (\text{C}_2 \lambda 5135) \rangle = -0.02 \pm 0.05$ dex (1σ , 23 stars). The C abundance was also estimated from the high-excitation C₁ λ 5380.3 line assuming $\log gf = -1.704$ (derived from an inverted solar analysis) and $E_\gamma = 2$. However, these abundances were found to be discrepant in the six coolest objects with those yielded by the C₂ features (see Fig. 5). For the remaining stars, there is a near-perfect agreement: $\langle \log \epsilon (\text{C}_1 \lambda 5380) - \log \epsilon (\text{C}_2) \rangle = +0.01 \pm 0.05$ dex (1σ , 18 stars). The origin of the discrepancy at low T_{eff} is unclear: departures from LTE (Fabbian et al. 2006), unrecognized blends (Luck & Heiter 2006, 2007), and/or granulation effects. In view of the problems plaguing the C₁ λ 5380 abundances, they are not discussed further. Although the departures from LTE affecting the C₂ features are largely unknown (Asplund 2005), the neglect of granulation should not lead to large errors (Dobrovolskas et al. 2013).

For the molecular feature at 6332.2 Å, seven CN(5,1) components were considered (with wavelengths from R. Smiljanic, private communication). The $\log gf$ values were taken from Jørgensen & Larsson (1990) with some adjustments based on the fit of the solar spectrum (see Table 3). Two Si I and Fe II lines at about 6331.95 Å lie in close vicinity of the CN feature. The oscillator strength of the stronger Si line ($\log gf = -2.64$) was inferred from an inverted solar analysis, while the value in VALD-2 was assumed for the Fe line ($\log gf = -2.071$; Raassen & Uylings 1998). Both the Si and the N abundances were adjusted during the fit. The Si abundances found systematically agreed within error with the mean values derived from the EWs. The atomic data for the lines of the A²Π-X²Σ⁺ system of CN(2,0) in the range 8002-8005 Å were taken from Jørgensen & Larsson (1990), but the wavelengths come from other sources (Wyller 1966; Tomkin et al. 1975; Boyarchuk et al. 1991; Barbay et al. 1992). The $\log gf$ value for Fe I λ 8002.58 was taken from Boyarchuk et al. (1991). Although the two indicators can only be used in a few stars, the N abundances agree well: $\langle \log \epsilon (\text{CN } 6332) - \log \epsilon (\text{CN } 8002-8004) \rangle = -0.07 \pm 0.07$ dex (1σ , 4 stars). As for the C₂ features, the magnitude of the NLTE effects for CN

Table 3. Atomic data for the CN(5,1) components included in the modelling of the CN λ 6332 feature.

Component	λ [Å]	LEP [eV]	$\log gf$
R ₂ (4)	6332.18	0.258	-2.258
R ₂ (3)	6332.18	0.256	-2.387
R ₂ (5)	6332.34	0.260	-2.433
R ₂ (2)	6332.34	0.255	-2.843
R ₂ (6)	6332.68	0.263	-2.804
R ₂ (1)	6332.68	0.254	-3.576
R ₂ (7)	6333.19	0.266	-2.879

is poorly known (Asplund 2005), and granulation is expected to have a limited impact (Dobrovolskas et al. 2013).

The ¹²C/¹³C isotopic ratio could be determined for four stars by fitting the ¹³CN feature at 8004.7 Å. For the other stars, we fixed this ratio to a value of 15, which may be regarded – as judged from the values obtained for these few stars and previous results in the literature (e.g., Smiljanic et al. 2009) – as representative of our sample. This choice has a very limited impact on the final results.

5.2.2. Line broadening parameters

The knowledge of the line broadening is needed to perform the spectral synthesis. The lines in red giants are broadened by stellar rotation and macroturbulent motions by a comparable amount. These two phenomena imprint a distinct, yet subtle, signature in the shape of the line profile that is best revealed through Fourier transforms applied to very high spectral resolution and S/N data (e.g., Gray & Brown 2006). In most cases, it is difficult with our observations to clearly disentangle the contribution of these two processes. The radial-tangential macroturbulence, ζ_{RT} , was therefore estimated from a calibration of this parameter across the HR diagram (Massarotti et al. 2008). The stellar luminosities were computed from the *Hipparcos* parallaxes (Table 1) and the bolometric corrections from the calibrations of Alonso et al. (1999). The CoRoT targets are relatively nearby ($d \lesssim 500$ pc), and $A_V = 0.2$ mag was assumed for all stars (no reddening was taken into account for the bright benchmark stars). For the NGC 6633 members, we assumed a distance of 375 pc (van Leeuwen 2009). For HD 170031, we adopted the value determined for HD 169370 ($\zeta_{\text{RT}} = 3.4$ km s⁻¹) in view of the similar physical parameters. Although these estimates of the stellar luminosity are uncertain (Sect. 2), they are sufficient for our purpose.

The projected rotational velocity, $v \sin i$, was subsequently derived by fitting a set of six relatively unblended Fe I lines in the vicinity of the Li doublet. The other free parameter was [Fe/H] (For all stars, the iron abundances found are identical within error of the mean values derived from the curve-of-growth analysis.). The only exception was α Boo, for which we used the values $\zeta_{\text{RT}} = 5.2$ and $v \sin i = 1.5$ km s⁻¹, as derived by Gray & Brown (2006) from Fourier techniques. The results we found ($\zeta_{\text{RT}} = 4.2$ and $v \sin i = 2.4$ km s⁻¹) lead to nearly identical line profile shapes. Our values for η Ser ($\zeta_{\text{RT}} = 3.8$ and $v \sin i = 1.5$ km s⁻¹) agree within error with those of Carney et al. (2008), which are based on a Fourier transform analysis. The microturbulent velocity was fixed to the values derived as described in Sect. 6 and listed in Table 6. Instrumental broadening at the wavelength of the feature of interest was assumed to be Gaussian and estimated from calibration lamps (As an illustration, see Table 1 for the values used for Li I λ 6708.). Finally, the

linear limb-darkening coefficients in the R band were taken from Claret (2000).

The $v \sin i$ values we derive are strongly tied to the choice of the adopted macroturbulence and are only meant to provide a good fit to the features synthesised. They are, therefore, surrounded by a large uncertainty, and these are not quoted. It is worth mentioning, however, that the value adopted for HD 50890 ($\sim 12.5 \text{ km s}^{-1}$ using a calibrated macroturbulence of 7.6 km s^{-1}) is much larger than that found for the other targets ($\leq 5 \text{ km s}^{-1}$). This suggests an unusually high rotation rate for a giant, although the crudeness of the calibration used to infer ζ_{RT} should be kept in mind. In view of the well-resolved nature of the line profiles in that particular case, an attempt was made to separate the contribution of each broadening mechanism through fitting two iron lines in the vicinity of the Li doublet (Fe I $\lambda 6703.6$ and 6705.1 \AA) with a grid of synthetic spectra computed for a wide range of $v \sin i$ and ζ_{RT} values. The other free parameter was the iron abundance (see Morel et al. 2013). Although there is a clear degeneracy in the determination of these two quantities, this analysis indeed supports a high rotational velocity of the order of 10 km s^{-1} (Fig. 6). The CNO and Li abundances were derived for this star using these best-fitting broadening parameters.

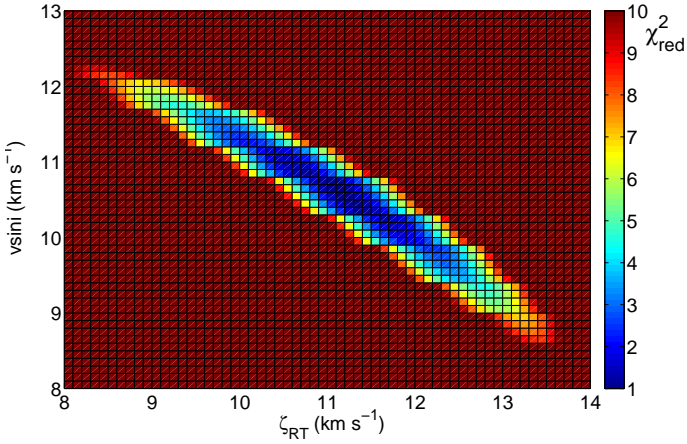


Fig. 6. Variation for the Fe I $\lambda 6705$ line in HD 50890 of the fit quality (colour-coded as a function of χ_{red}^2) for different combinations of $v \sin i$ and ζ_{RT} . The best fit is found for $\zeta_{\text{RT}} = 11.1$ and $v \sin i = 10.6 \text{ km s}^{-1}$ (and $[\text{Fe}/\text{H}] = +0.05$). Similar results are obtained for Fe I $\lambda 6703$. Note that the fit quality of the analysis that made use of a calibrated ζ_{RT} of 7.6 km s^{-1} (and which led to $v \sin i = 12.5 \text{ km s}^{-1}$) cannot be judged from this figure because the adopted metallicity is different.

6. Determination of stellar parameters

The model parameters (T_{eff} , $\log g$, ξ , $[\text{Fe}/\text{H}]$, and abundances of the α elements) were iteratively modified until all the following conditions were simultaneously fulfilled: (1) the Fe I abundances exhibit no trend with lower excitation potential (LEP) or reduced EW (the logarithm of the EW divided by the wavelength of the transition). Our selected neutral iron lines span a wide range in LEP and strength and are therefore well suited to constrain both the temperature and the macroturbulence; (2) the abundances derived from the Fe I and Fe II lines are identical; and (3) the Fe and α -element abundances are consistent with the values adopted for the model atmosphere. The number of iron lines

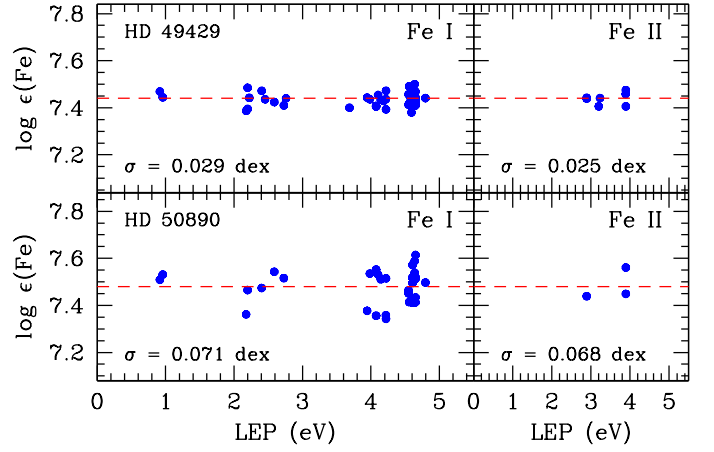


Fig. 7. Abundances derived from the Fe I and Fe II lines for HD 49429 and HD 50890 as a function of the LEP. The horizontal dashed line indicates the mean iron abundance.

used ranges from 33 to 63 for Fe I and from 3 to 9 for Fe II. The typical line-to-line scatter of the Fe abundances (either for Fe I or Fe II) is 0.05 dex. Figure 7 shows the variation of the Fe abundances as a function of the LEP for two stars showing amongst the lowest and largest scatters.

The ODFs and Rosseland opacity tables were chosen according to the microturbulence and Fe abundance (rounded to the nearest 0.1 dex), as derived from the spectral analysis. Furthermore, the α -element abundance of the model varied depending on $[\text{Fe}/\text{H}]$, which follows the same convention as adopted for the MARCS suite of models (e.g., $[\alpha/\text{Fe}] = +0.2$ for $[\text{Fe}/\text{H}] = -0.4$; Gustafsson et al. 2008). If necessary, the ODFs for the appropriate Fe and α -element abundances were linearly interpolated from a pre-calculated grid available online.⁷

As discussed in Sect. 4, the seismic gravities are likely not only more precise but also more accurate than the values derived from the ionisation balance of iron. We therefore repeated the analysis after fixing the gravity of the models to this value. Such an approach is now routinely implemented in spectroscopic studies of seismic targets (e.g., Batalha et al. 2011; Carter et al. 2012; Thygesen et al. 2012; Huber et al. 2013) and is expected to provide more robust estimates of the physical parameters and ultimately chemical abundances. The temperature was also determined from Fe excitation balance. A change in $\log g$ of 0.1 dex typically leads to variations in T_{eff} of 15 K and in $[\text{Fe}/\text{H}]$ of 0.04 dex. Similar figures are obtained for solar-like stars (Torres et al. 2012; Huber et al. 2013). The good agreement in our case between the two sets of $\log g$ values (see below) only implies small adjustments for T_{eff} ($\leq 30 \text{ K}$) and the abundances (≤ 0.1 dex). A more general discussion including results for *Kepler* targets is presented in Morel (2014).

Although ionisation balance of iron is usually fulfilled within the errors, the formal mean iron abundance yielded by the Fe I and Fe II lines may differ by up to 0.18 dex (and on average by 0.07 dex) when the gravity is held fixed to the seismic value. There is therefore an ambiguity as to which metallicity value should be eventually adopted. As the Fe I lines are known to be more prone to departures from LTE, it may be argued that the mean Fe II-based abundance is a better proxy of the stellar metallicity (e.g., Thygesen et al. 2012). However, the abundances yielded by the Fe II lines are also affected by a number

⁷ For more details, see: <http://wwwuser.oat.ts.astro.it/castelli/odfnew.html>.

of caveats in red giants: (1) the features are only usually a few, difficult to measure, and potentially more affected by blends; (2) they are very sensitive to errors in the effective temperature (varying T_{eff} by 50 K while keeping the gravity fixed typically changes the Fe I and Fe II abundances by 0.01-0.02 and 0.06 dex, respectively; see also Ramírez & Allende Prieto 2011); (3) they suffer, as with the Fe I lines (and perhaps even more according to models), from the neglect of granulation effects (Collet et al. 2007; Kučinskas et al. 2013; see also fig.15 of Dobrovolskas et al. 2013). In view of the uncertainties plaguing both the Fe I and Fe II abundances, we consider in the following that the iron content is given by the average of the values yielded by these two ions.

7. Computation of uncertainties

The uncertainties affecting our results are schematically two kinds: statistical and systematic. We tried to incorporate both in the total uncertainty budget, assuming that the choices of the line list and the set of model atmospheres were the main sources of systematic uncertainties.

7.1. Physical parameters

To assess the uncertainties in the physical parameters associated to the choice of the diagnostic lines, we repeated the analysis using the line lists of Morel et al. (2003, 2004) and Hekker & Meléndez (2007) described in Sect. 5.1. The standard deviation of the results was about 40 K for T_{eff} , 0.10 dex for $\log g$, and 0.04 km s⁻¹ for ξ . Four stars were not observed with HARPS or ELODIE, but with instruments offering a wider wavelength coverage (FEROS and KPNO échelle). However, re-analysing these stars by only considering the lines covered by HARPS leads to very small differences.

The uncertainties arising from the choice of the model atmosphere were estimated by analysing a number of stars using plane-parallel MARCS (Gustafsson et al. 2008) and Kurucz models computed with different assumptions regarding their metal content. Namely, we repeated the analysis by varying the input metallicity and α enhancement of the models by their typical uncertainty ($\Delta[\text{Fe}/\text{H}] = 0.1$ and $\Delta[\alpha/\text{Fe}] = 0.2$ dex). Furthermore, we assumed different treatments for the convection (adopting various ratios of the mixing length to scale height or incorporating overshooting). A few stars (α Boo, ϵ Oph, and ξ Hya) were analysed with spherical MARCS models, but small differences in terms of atmospheric parameters were found with respect to plane-parallel Kurucz models (see also Carlberg et al. 2012). As expected, the largest changes by far were found for the low-gravity star α Boo with T_{eff} and $\log g$ larger by 55 K and 0.13 dex, respectively. In contrast, extremely similar results were found for ϵ Oph and ξ Hya that are more representative of our sample. These relatively small differences, which remain within the uncertainties, can be explained by the similar atmospheric structure for the range of parameters spanned by our targets (Gustafsson et al. 2008). Very small variations in the iron abundances were also found in accordance with previous studies (Heiter & Eriksson 2006). Once again, α Boo deviated the most, but $[\text{Fe}/\text{H}]$ was only 0.04 dex larger. In addition, we experimented with the MARCS models that were moderately contaminated by CN-cycled material (as is the case for most of our targets as discussed below) but found negligible differences with respect to the models that assume a scaled-solar mixture.

We finally obtain the following figures for the systematic uncertainties: 70 K for T_{eff} , 0.15 dex for $\log g$, and 0.05 km s⁻¹ for

Table 4. Uncertainty budget for the abundances derived from the EWs in the case of HD 175679.

	σ_{int}	$\sigma_{T_{\text{eff}}}$	$\sigma_{\log g}$	σ_{ξ}	$\sigma_{\text{normalisation}}$	σ_{total}
$\Delta[\text{Fe}/\text{H}]$	0.05	+0.05	+0.00	-0.01	+0.07	0.10
$\Delta[\text{O I triplet}/\text{Fe}]$	0.05	-0.07	+0.11	-0.01	+0.04	0.15
$\Delta[\text{Na}/\text{Fe}]$	0.03	-0.02	-0.02	+0.01	-0.01	0.05
$\Delta[\text{Mg}/\text{Fe}]$	0.07 ^a	-0.04	-0.03	-0.01	-0.01	0.09
$\Delta[\text{Al}/\text{Fe}]$	0.07	-0.02	-0.02	+0.02	+0.01	0.08
$\Delta[\text{Si}/\text{Fe}]$	0.08	-0.04	+0.03	+0.01	+0.01	0.10
$\Delta[\text{Ca}/\text{Fe}]$	0.05	-0.01	-0.02	-0.01	+0.00	0.06
$\Delta[\text{Sc}/\text{Fe}]$	0.07 ^a	+0.05	+0.09	+0.03	+0.00	0.13
$\Delta[\text{Ti}/\text{Fe}]$	0.07 ^a	+0.01	-0.01	+0.03	+0.03	0.09
$\Delta[\text{Cr}/\text{Fe}]$	0.14	+0.00	-0.02	+0.01	-0.01	0.15
$\Delta[\text{Co}/\text{Fe}]$	0.07 ^a	+0.01	+0.01	+0.02	+0.00	0.08
$\Delta[\text{Ni}/\text{Fe}]$	0.04	-0.01	+0.02	+0.00	+0.00	0.05
$\Delta[\text{Ba}/\text{Fe}]$	0.07 ^a	+0.02	+0.08	-0.02	+0.00	0.11

Notes. The first column gives the line-to-line scatter. The quantities $\sigma_{T_{\text{eff}}}$, $\sigma_{\log g}$, and σ_{ξ} give the uncertainties associated to the following changes in the atmospheric parameters: $\Delta T_{\text{eff}} = +80$ K, $\Delta \log g = +0.18$ dex, and $\Delta \xi = +0.07$ km s⁻¹. Note that the two other parameters were simultaneously adjusted to fulfil excitation/ionisation equilibrium of iron or to have the Fe I abundances that are independent of the line strength. Finally, $\sigma_{\text{normalisation}}$ provides the changes associated to a continuum level shifted upwards by 1% (These values were adopted for all the stars in our sample.). ^(a) Arbitrary value.

ξ . With the gravity fixed to the seismic value, this reduces to 35 K for T_{eff} and 0.025 km s⁻¹ for ξ .

The statistical uncertainties are first related to the errors made when fulfilling excitation and ionisation equilibrium of the iron lines (T_{eff} and $\log g$) or when constraining the Fe I abundances to be independent of the line strength (ξ). To estimate the uncertainty in T_{eff} , for instance, we considered the range over which the slope of the relation between the Fe I abundances and the LEP is consistent with zero within the uncertainties. As the parameters of the model (T_{eff} , $\log g$, and ξ) are interdependent, changes in one of these parameters are necessarily accompanied by variations in the other two. Two of these parameters were therefore adjusted, while the third one was varied by the relevant uncertainty. In addition, to assess the uncertainties associated to the placement of the continuum level, we re-estimated the parameters of HD 175679 after shifting the continuum upwards by 1%. This led to negligible variations for T_{eff} and ξ , while $\log g$ was 0.03 dex lower. These figures were considered as being representative and adopted for all the stars in our sample.

The final uncertainty was taken as the quadratic sum of the statistical and systematic errors (Because of the small scatter of the Fe abundances, the latter are often found to dominate.).

7.2. Chemical abundances

To investigate the sensitivity of the abundances obtained from curve-of-growth techniques to changes in the physical parameters, we repeated the analysis by varying each parameter by its global (systematic and statistical) uncertainty defined above. We proceeded as above to estimate the uncertainties related to the placement of the continuum level. As expected, this has a noticeable effect on $[\text{Fe}/\text{H}]$ but a much lower impact on the abundance ratios with respect to iron. Finally, the line-to-line scatter, σ_{int} , was quadratically summed to these values to obtain the final uncertainty (We assumed a rather generous value of 0.07 dex when the abundance was based on a single line.). The uncertainty budget is described in the case of HD 175679 in Table 4.

For the abundances obtained through spectral synthesis, the same procedure as above was applied to HD 175679, and the uncertainties were taken as representative of the whole sample.

The only exception was $^{12}\text{C}/^{13}\text{C}$ for which the sensitivity against the placement of the continuum was estimated on a star-to-star basis. It should be noted that this ratio is largely insensitive to the exact choice of the parameters (see Smiljanic et al. 2009). The abundances of all elements other than Li and CNO were updated and fixed in the synthesis to the values obtained with the new set of parameters. As the fit quality was evaluated by eye, we incorporated a typical error associated to this procedure. For [O I] $\lambda 6300$, varying the nickel abundance (and therefore the contamination of the blended Ni feature) within its uncertainty led to negligible changes. Finally, a typical uncertainty of 0.1 eV in the dissociation energy of the C_2 and CN molecules was also taken into account in the total uncertainty budget. Once again, the final uncertainty was taken as the quadratic sum of all these sources of errors (see Table 5). The uncertainties in the Li and CNO abundances associated to the use of 1D LTE models are discussed in Sect. 5.2.1.

The physical parameters are provided in Table 6, while the chemical abundances are given in Tables A.4 and A.5. Table A.6 presents the logarithmic CNO abundance ratios.

8. Validation of results

8.1. Physical parameters

The reliability of our spectroscopic gravities can be investigated for 17 stars in our sample by comparing with the independent estimates provided by asteroseismology (As discussed in Sect. 4, these values are mainly a function of the seismic observables and are only very weakly dependent on the T_{eff} assumed.). As shown in Fig. 8, these two sets of values agree well: $\langle \log g [\text{spectroscopy}] - \log g [\text{seismology}] \rangle = +0.04 \pm 0.13$ dex. There is also no clear evidence of a trend as a function of the seismic gravity, effective temperature, or metallicity. None of the slopes is statistically different from zero.

The five bright, well-studied red giants offer an opportunity to compare our results to the numerous ones already available in the literature. More importantly, it also allows us to investigate possible differences between our T_{eff} values and the completely independent (and more likely accurate) ones derived using interferometric techniques. For α Boo, these measurements show a very high level of consistency, where $T_{\text{eff}} = 4303 \pm 47$ (Quirrenbach et al. 1996), 4290 ± 30 (Griffin & Lynas-Gray 1999), and 4295 ± 26 K (Lacour et al. 2008). We adopt the last value in the following. The other stars only have a single value available in the literature: η Ser (4925 ± 40 K; Mérand et al. 2010), ϵ Oph (4912 ± 25 K; Mazumdar et al. 2009), ξ Hya (4984 ± 54 K; Bruntt et al. 2010), and β Aql (4986 ± 111 K; Bruntt et al. 2010). Figure 9 shows a comparison between our $\log g$ and T_{eff} values and those derived from seismic and interferometric data, respectively. Also shown are the previous results in the literature, which are summarised in Table A.1 (certainly not exhaustive for α Boo). We restrict ourselves to studies carried out over the past ~ 25 years to select analyses based on higher-quality observational material and improved analysis techniques. We also make the distinction between fundamental parameters that are derived using similar methods as used here (excitation and ionisation equilibrium of Fe lines) or determined by other means. Our effective temperatures agree to the interferometric values within the uncertainties in all cases. Observations with the CHARA Array interferometer recently yielded $T_{\text{eff}} = 4577 \pm 60$ K for HD 50890 (Baines et al. 2013). This is about 130 K cooler than our estimate.

Table 6. Atmospheric parameters of the targets.

	T_{eff} [K]	$\log g$ [cgs]	ξ [km s $^{-1}$]	[Fe/H]
HD 40726	5230 \pm 80	2.71 \pm 0.18	1.67 \pm 0.07	+0.05 \pm 0.11
HD 42911	4905 \pm 80	2.80 \pm 0.20	1.42 \pm 0.07	+0.12 \pm 0.11
HD 43023	5065 \pm 80	2.93 \pm 0.19	1.38 \pm 0.07	-0.05 \pm 0.10
HD 45398	4155 \pm 85	1.50 \pm 0.23	1.50 \pm 0.08	-0.15 \pm 0.14
HD 49429	5085 \pm 75	3.01 \pm 0.17	1.33 \pm 0.06	-0.06 \pm 0.10
HD 49566	5170 \pm 75	3.01 \pm 0.17	1.39 \pm 0.06	-0.04 \pm 0.10
	5185 \pm 50	[2.89 \pm 0.04]	1.42 \pm 0.04	-0.08 \pm 0.09
HD 50890	4730 \pm 95	1.85 \pm 0.26	1.98 \pm 0.10	-0.02 \pm 0.13
	4710 \pm 75	[2.07 \pm 0.08]	1.98 \pm 0.09	+0.06 \pm 0.12
HD 169370	4520 \pm 85	2.31 \pm 0.22	1.42 \pm 0.07	-0.27 \pm 0.13
	4520 \pm 60	[2.32 \pm 0.04]	1.42 \pm 0.06	-0.26 \pm 0.10
HD 169751	4900 \pm 80	2.72 \pm 0.19	1.23 \pm 0.07	+0.00 \pm 0.11
	4910 \pm 55	[2.67 \pm 0.07]	1.24 \pm 0.05	-0.02 \pm 0.10
HD 170008	5130 \pm 75	3.43 \pm 0.17	1.04 \pm 0.07	-0.35 \pm 0.10
	5130 \pm 50	[3.45 \pm 0.04]	1.04 \pm 0.05	-0.34 \pm 0.09
HD 170031	4535 \pm 85	2.41 \pm 0.21	1.43 \pm 0.08	-0.01 \pm 0.14
	4515 \pm 65	[2.47 \pm 0.09]	1.41 \pm 0.07	+0.04 \pm 0.11
HD 171427	4875 \pm 90	1.94 \pm 0.27	2.29 \pm 0.10	-0.02 \pm 0.13
HD 175294	4950 \pm 85	2.85 \pm 0.20	1.60 \pm 0.08	+0.25 \pm 0.12
HD 175679	5150 \pm 80	2.94 \pm 0.18	1.58 \pm 0.07	+0.11 \pm 0.10
	5180 \pm 50	[2.66 \pm 0.11]	1.63 \pm 0.06	+0.02 \pm 0.10
HD 178484	4450 \pm 85	1.90 \pm 0.23	1.58 \pm 0.07	-0.32 \pm 0.12
	4440 \pm 60	[1.96 \pm 0.07]	1.58 \pm 0.06	-0.29 \pm 0.10
HD 181907	4705 \pm 90	2.44 \pm 0.23	1.59 \pm 0.08	-0.11 \pm 0.13
	4725 \pm 65	[2.35 \pm 0.04]	1.61 \pm 0.06	-0.15 \pm 0.12
HD 170053	4315 \pm 90	1.72 \pm 0.23	1.69 \pm 0.08	-0.14 \pm 0.13
	4290 \pm 65	[1.85 \pm 0.16]	1.68 \pm 0.07	-0.03 \pm 0.12
HD 170174	5035 \pm 80	2.74 \pm 0.19	1.55 \pm 0.07	-0.01 \pm 0.11
	5055 \pm 55	[2.56 \pm 0.05]	1.58 \pm 0.06	-0.07 \pm 0.10
HD 170231	5150 \pm 80	2.96 \pm 0.19	1.45 \pm 0.08	+0.04 \pm 0.11
	5175 \pm 55	[2.74 \pm 0.06]	1.49 \pm 0.06	-0.03 \pm 0.10
α Boo	4255 \pm 85	1.45 \pm 0.23	1.77 \pm 0.09	-0.67 \pm 0.13
	4260 \pm 60	[1.42 \pm 0.08]	1.77 \pm 0.08	-0.69 \pm 0.11
η Ser	4915 \pm 80	3.07 \pm 0.18	1.14 \pm 0.07	-0.21 \pm 0.10
	4935 \pm 50	[3.00 \pm 0.05]	1.17 \pm 0.05	-0.24 \pm 0.09
ϵ Oph	4935 \pm 85	2.66 \pm 0.21	1.42 \pm 0.07	-0.03 \pm 0.11
	4940 \pm 55	[2.64 \pm 0.06]	1.43 \pm 0.06	-0.04 \pm 0.10
ξ Hya	5080 \pm 75	2.96 \pm 0.17	1.32 \pm 0.06	+0.13 \pm 0.10
	5095 \pm 50	[2.88 \pm 0.05]	1.34 \pm 0.05	+0.10 \pm 0.09
β Aql	5100 \pm 80	3.56 \pm 0.17	0.97 \pm 0.07	-0.21 \pm 0.11
	5110 \pm 50	[3.53 \pm 0.04]	0.99 \pm 0.06	-0.22 \pm 0.09

Notes. When available, the second row shows the results with the surface gravity fixed to the seismic value for each star (given in square brackets).

Our results may suffer from the neglect of granulation and departures from LTE, but the checks described above suggest that the parameters determined from spectroscopy are reasonably accurate. For the range of parameters spanned by our targets (especially since they have a near-solar metallicity), departures from LTE are expected to have a limited impact on the temperature and gravity derived from excitation and ionisation balance (Lind et al. 2012). Detailed calculations (Bergemann et al. 2012; Lind et al. 2012) available through the INSPECT database⁸ indeed show that the NLTE corrections only amount to an average of 0.03 dex for a number of Fe I and Fe II lines in our list that span a relatively wide range in strength and LEP. As shown by state-of-the-art 3D hydrodynamical simulations, the use of classical model atmospheres may be a more questionable assumption, although, once again, the problem is much more acute at low metallicities according to the calculations presented by Collet

⁸ See www.inspect-stars.net.

Table 5. Uncertainty budget for the abundances of the mixing indicators in the case of HD 175679.

	σ_{int}	σ_{Teff}	σ_{logg}	σ_{ξ}	$\sigma_{\text{normalisation}}$	σ_{fit}	σ_{Ni}	σ_{D_0}	σ_{total}
$\Delta \log \epsilon(\text{O})$	0.05 ^a	+0.11	+0.08	+0.04	+0.06	0.03	+0.01	+0.00	0.17
$\Delta[\text{O}/\text{Fe}]$	0.05 ^a	+0.06	+0.08	+0.05	+0.06	0.03	+0.01	+0.00	0.14
$\Delta \log \epsilon(\text{C}_2 \text{ 5086})$...	+0.06	+0.03	+0.02	+0.04	0.03	+0.00	+0.04	0.10
$\Delta \log \epsilon(\text{C}_2 \text{ 5135})$...	+0.06	+0.04	+0.02	+0.04	0.03	+0.00	+0.04	0.10
$\Delta \log \epsilon(\text{C}_2)$	0.03	+0.06	+0.04	+0.02	+0.04	0.03	+0.00	+0.04	0.11
$\Delta[\text{C}/\text{Fe}]$	0.03	+0.01	+0.04	+0.03	+0.04	0.03	+0.00	+0.04	0.09
$\Delta \log \epsilon(\text{CN } 6332)$...	+0.08	-0.01	+0.03	+0.04	0.03	+0.00	+0.08	0.13
$\Delta \log \epsilon(\text{CN } 8003)$...	+0.08	+0.00	+0.03	+0.06	0.03	+0.00	+0.09	0.14
$\Delta \log \epsilon(\text{N})$	0.05	+0.08	-0.01	+0.03	+0.05	0.03	+0.00	+0.08	0.14
$\Delta[\text{N}/\text{Fe}]$	0.05	+0.03	-0.01	+0.04	+0.05	0.03	+0.00	+0.08	0.13
$\Delta[\text{N}/\text{C}]$	0.06	+0.02	-0.04	+0.01	+0.01	0.04	+0.00	+0.04	0.10
$\Delta[\text{N}/\text{O}]$	0.07	-0.03	-0.09	-0.01	-0.01	0.04	-0.01	+0.08	0.15
$\Delta[\text{C}/\text{O}]$	0.06	-0.05	-0.05	-0.02	-0.02	0.04	-0.01	+0.04	0.12
$\Delta^{12}\text{C}/^{13}\text{C}$...	-0.3	-0.2	+0.00	-5	1	+0.00	+0.00	5.1
$\Delta[\text{Li}/\text{H}]$	0.05 ^a	+0.09	-0.04	+0.03	+0.05	0.05	+0.00	+0.00	0.13

Notes. The first column gives the line-to-line scatter. The quantities σ_{Teff} , σ_{logg} , and σ_{ξ} give the uncertainties associated to the following changes in the atmospheric parameters: $\Delta T_{\text{eff}} = +80$ K, $\Delta \log g = +0.18$ dex, and $\Delta \xi = +0.07$ km s⁻¹. Note that the two other parameters were simultaneously adjusted to fulfil excitation/ionisation equilibrium of iron or to have the Fe I abundances that are independent of the line strength. The uncertainty associated to a continuum level shifted upwards by 1% is provided by $\sigma_{\text{normalisation}}$. As the fit quality was evaluated by eye, σ_{fit} gives the rough uncertainty associated to this procedure. The error resulting from a lowering of the Ni abundance by its uncertainty (0.05 dex) is given by σ_{Ni} . Finally, the effect of lowering the adopted dissociation energy of the C₂ and CN molecules by 0.1 eV is given by σ_{D_0} . ^(a) Arbitrary value.

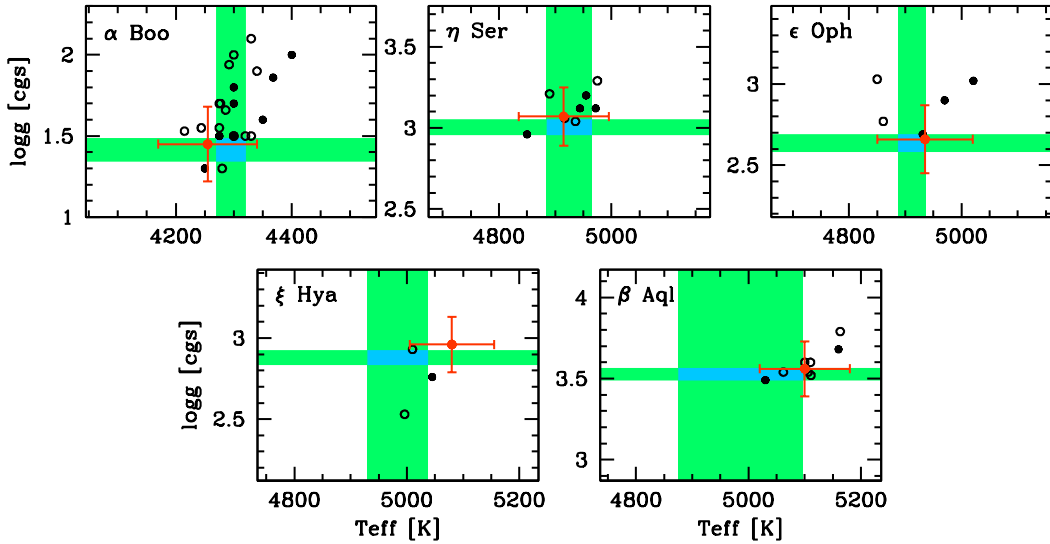


Fig. 9. Comparison for the stars used for validation between our T_{eff} and $\log g$ values (red) and those derived from interferometric and seismic data (green areas delimiting the 1- σ error bars). Black dots: previous results from the literature (filled and open symbols: parameters derived as in the present study or using different techniques, respectively). Further details about the literature data can be found in the appendix.

et al. (2007). The good level of consistency achieved between our spectroscopic parameters and independent estimates might indicate that the effect of granulation is not as severe at near-solar metallicity as anticipated by these particular models (see Dobrovolskas et al. 2013).

We show the few temperatures and gravities previously obtained for the CoRoT targets in Table 7. Our estimates and the mean values in the literature agree well. Significant differences are, however, found with respect to Valenti & Fischer (2005) and Liu et al. (2010) for HD 170174 and HD 175679, respectively. The results of Valenti & Fischer (2005) are based on spectral synthesis techniques, while Liu et al. (2010) used photometric indices and isochrone fitting.

As a final validation test, our spectrum of HD 181907 was analysed with an automated tool by making use of the EWs of iron lines and MARCS model atmospheres (see Valentini et al. 2013). The following results were obtained: $T_{\text{eff}} = 4679 \pm 54$ K, $\log g = 2.28 \pm 0.11$, $\xi = 1.35 \pm 0.09$ km s⁻¹, and $[\text{Fe}/\text{H}] = -0.17 \pm 0.07$. Fixing the gravity to the seismic value does not significantly change the results: $T_{\text{eff}} = 4735 \pm 46$ K, $\xi = 1.48 \pm 0.06$ km s⁻¹, and $[\text{Fe}/\text{H}] = -0.15 \pm 0.05$. These results are close to ours and indicate that the parameters obtained for this star are robust.

Table 7. Previous results obtained in the literature for the CoRoT targets.

Star	T_{eff} [K]		log g [cgs]		ξ [km s $^{-1}$]	[Fe/H]	[Li/H] LTE	[C/Fe]	[N/Fe]	[O/Fe]	[Na/Fe]	Ref.
	Value	Method	Value	Method								
HD 43023	5065±80	E	2.93±0.19	I	1.38±0.07	-0.05±0.10	<-1.40	-0.23	+0.39	-0.02	+0.10	
	5140±80	E	3.10±0.20	I	1.41±0.20	+0.04±0.15	1
	5105±100	E	3.08±0.10	I	1.50±0.30	-0.06±0.12	<-0.46	-0.22	+0.22	+0.17	+0.11	2
	5005±75	E	2.71±0.15	I	1.30±0.08	-0.10±0.08	...	-0.20	+0.06	3 ^a
	5027±100	P	2.97±0.15	LMT	...	+0.06±0.15	4
	4994±100	LDR	2.40±0.20	I	1.3±0.2	-0.13±0.12	<-0.59	-0.27	+0.28	+0.00	+0.02 ^b	...
5005	S	2.68	S	...	-0.04	6
HD 50890	4730±95	E	1.85±0.26	I	1.98±0.10	-0.02±0.13	-0.07	-0.40	+0.58	-0.24	+0.51	
	4710±75	E	[2.07±0.08]	A	1.98±0.09	+0.06±0.12	-0.13	-0.43	+0.57	-0.20	+0.41	
	4665±200	E	1.4±0.3	I	...	-0.18±0.14	7
HD 169370	4520±85	E	2.31±0.22	I	1.42±0.07	-0.27±0.13	-1.41	-0.03	+0.06	+0.08	+0.03	
	4520±60	E	[2.32±0.04]	A	1.42±0.06	-0.26±0.10	-1.41	-0.04	+0.05	+0.07	+0.02	
	4460±70	E	2.3±0.2	I	1.3±0.2	-0.17±0.10	8
	4547	LDR	9
HD 170053	4315±90	E	1.72±0.23	I	1.69±0.08	-0.14±0.13	+0.11	-0.15	+0.42	-0.04	+0.27	
	4290±65	E	[1.85±0.16]	A	1.68±0.07	-0.03±0.12	+0.06	-0.18	+0.43	-0.06	+0.13	
	4370±60	E	1.80±0.26	I	1.51±0.08	+0.04±0.10	...	-0.17	+0.38	-0.17	-0.01 ^b	10
HD 170174	5035±80	E	2.74±0.19	I	1.55±0.07	-0.01±0.11	-0.48	-0.20	+0.46	-0.03	+0.20	
	5055±55	E	[2.56±0.05]	A	1.58±0.06	-0.07±0.10	-0.45	-0.17	+0.52	-0.05	+0.28	
	5015±60	E	2.85±0.26	I	1.44±0.08	+0.11±0.11	...	-0.19	+0.45	-0.12	-0.03 ^b	10
	4979±72	E	2.75±0.12	I	1.58±0.10	-0.08±0.10	11
	5245±44	S	3.11±0.06	S	0.85	+0.35±0.03	+0.07	12
HD 175679	5150±80	E	2.94±0.18	I	1.58±0.07	+0.11±0.10	+0.15	-0.24	+0.46	-0.05	+0.17	
	5180±50	E	[2.66±0.11]	A	1.63±0.06	+0.02±0.10	+0.20	-0.19	+0.56	-0.09	+0.29	
	4844±100	P	2.59±0.10	LMT	1.4±0.2	-0.15±0.10	...	+0.04	...	-0.02	+0.17	13

Notes. The rows in boldface show the results of this study (When available, the second one shows the results with the surface gravity fixed to the seismic value, which is given in square brackets for each star.). The abundances were rescaled to our adopted solar values when appropriate and whenever these were not quoted in the original paper. **E**: from excitation equilibrium of the Fe I lines; **I**: from ionisation equilibrium of Fe; **P**: from photometric data; **LMT**: from estimates of the luminosity, mass, and effective temperature; **S**: from spectral synthesis; **LDR**: from line-depth ratios; **A**: from asteroseismology. References. (1) Hekker & Meléndez 2007; (2) Luck & Heiter 2007; (3) Takeda et al. 2008; (4) Zhao et al. 2001; (5) Mishenina et al. 2006; (6) Soubiran et al. 2008; (7) Baudin et al. 2012; (8) da Silva et al. 2006; (9) Biazzo et al. 2007; (10) Smiljanic et al. 2009; (11) Santos et al. 2009 (based on the line list of Hekker & Meléndez 2007); (12) Valenti & Fischer 2005; (13) Liu et al. 2010. ^a As Takeda et al. caution, their oxygen abundances may not be reliable. ^(b) NLTE value.

8.2. Chemical abundances

For the sake of brevity, we restrict ourselves here to only discuss the metallicity scale and the chemical species used as a probe of mixing (Li, CNO, and Na).

As seen in Table A.1, our metallicities for the benchmark stars and those in the literature agree generally well. The cause of the rather low value we obtain for α Boo is unclear, but it is not attributable to a grossly overestimated microturbulence.

Not surprisingly in view of the different parameters adopted (see above), our metallicities for two CoRoT targets (Table 7) are at odds with those of Valenti & Fischer (2005) and Liu et al. (2010). As is the case for η Ser (Table A.1), the higher [Fe/H] of Valenti & Fischer (2005) may stem for the most part from an adopted microturbulence that is too low. We obtain a metallicity that is higher at the ~ 0.2 dex level for HD 50890 compared to Baudin et al. (2012), but their gravity was poorly constrained.

Stars in the young open cluster NGC 6633 offer an opportunity to assess the reliability of our metallicities because the values we obtain for the three likely members should be identical within the uncertainties. Santos et al. (2009) and Smiljanic et al. (2009) obtained -0.08 and $+0.07$ for the mean metallicity of the cluster based on the analysis of three and two red giants, respectively. Table 7 shows a comparison between our results and those they obtained for the two stars in common: HD 170053 and HD 170174.⁹ On the other hand, Jeffries et al. (2002) obtained [Fe/H] = -0.10 ± 0.08 for 10 FG dwarfs and determined

that NGC 6633 is significantly more metal poor than the Hyades (by ~ 0.21 dex) or the Pleiades (by ~ 0.07 dex), which should be regarded as a more robust result. We obtain -0.04 ± 0.04 for the mean metallicity of the cluster when considering the seismic constraints for the three likely members. It could be noted that HD 170053 is no longer discrepant in terms of iron content when the gravity is fixed to the more accurate seismic value (see Table 6).

With regard to the Li, CNO, or Na abundances, there is a good overall agreement for the benchmark stars with respect to previous studies (listed in Table A.1). There is, however, some evidence of slightly larger C abundances in our case compared to Bruntt et al. (2010) for three stars in common. Our upper limits for the Li abundance in two stars (η Ser and β Aql) also appear inconsistent with their report of a detection. Our value for ξ Hya is also ~ 0.3 dex lower.

To the best of our knowledge, only four CoRoT targets have previous determinations of the abundances of these elements (HD 43023, HD 170053, HD 170174, and HD 175679). Although there are generally only small differences compared to the literature data (Table 7), three discrepancies are worth pointing out: (1) the larger C abundance found in HD 175679 by Liu et al. (2010); (2) the differences at the ~ 0.2 dex level with the N and O abundances of Luck & Heiter (2007) for HD 43023; and (3) the lower [Na/Fe] ratios reported by Smiljanic et al. (2009) for two stars in NGC 6633. This may not arise from differences in the adopted parameters (see Table 4), and the cause of this dis-

⁹ We consider the results of Santos et al. (2009) based on the line list of Hekker & Meléndez (2007), which, as they discuss, is more appropriate for red giants. Their metallicities were also rescaled to the value they inferred from the analysis of a solar reflection spectrum.

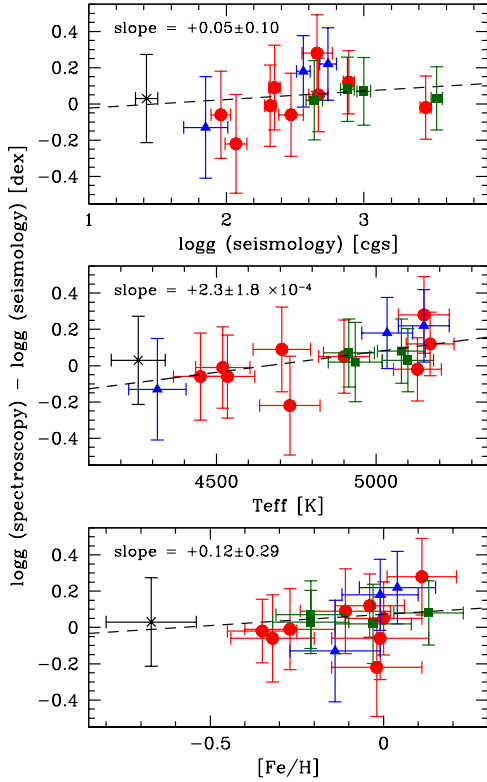


Fig. 8. Comparison between the surface gravities derived from ionisation balance of iron and from seismic data, as a function of the seismic $\log g$, T_{eff} , and $[\text{Fe}/\text{H}]$ (red dots: CoRoT targets, blue triangles: stars in NGC 6633, black cross: α Boo, green squares: other stars used for validation). The fits weighted by the inverse variance are shown as dashed lines, and the slopes are indicated.

agreement is unclear. Our abundances can be revised downwards by ~ 0.08 dex if we adopt their $\log gf$ values and take into account their NLTE corrections. However, using their EWs would lead to abundances higher by ~ 0.09 dex.

Smiljanic et al. (2009) report a $^{12}\text{C}/^{13}\text{C}$ isotopic ratio of 18 ± 8 and 21 ± 7 for HD 170053 and HD 170174, respectively, which we are unable to confirm because no ^{13}C lines are covered by our observations. The only point of comparison for this quantity is provided by α Boo. Our value ($^{12}\text{C}/^{13}\text{C} = 8 \pm 1$) closely agrees with those in the literature, which range from 6 to 10 (e.g., Pilachowski et al. 1997; Pavlenko 2008; Abia et al. 2012).

9. Correction for the chemical evolution of the Galaxy

As shown in Fig. 10, the abundance ratios with respect to iron of several elements (e.g., Ca) exhibit a clear trend with $[\text{Fe}/\text{H}]$. The larger abundance ratios, which are observed as $[\text{Fe}/\text{H}]$ decreases, is a well-known feature of Galactic disk stars and arises from the different relative proportion of Type Ia/II supernovae yields and the various amounts of material lost by stellar winds from AGB or massive stars along the history of the Galaxy (In contrast, the iron-peak elements closely follow Fe as expected.). This behaviour is also observed in our sample for some mixing indicators and indicates that these abundances are not only affected by mixing processes but also – and perhaps to a larger extent – by the chemical evolution of the Galaxy. To disentangle the contribution of these two phenomena to first order, we corrected these abundances by removing the metallicity trend found

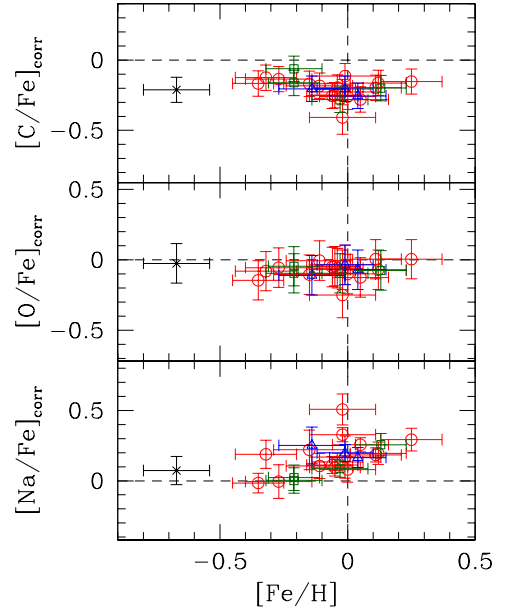


Fig. 11. Corrected abundance ratios with respect to iron for C, O, and Na, as a function of $[\text{Fe}/\text{H}]$. The results have been obtained using the spectroscopic gravities. Same symbols as in Fig. 8.

in dwarfs of the Galactic thin disk by Ecuivillon et al. (2004a, 2006) for C and O and by Reddy et al. (2003) for Na, as follows:

$$[\text{C}/\text{Fe}]_{\text{corr}} = [\text{C}/\text{Fe}] + 0.39[\text{Fe}/\text{H}], \quad (4)$$

$$[\text{O}/\text{Fe}]_{\text{corr}} = [\text{O}/\text{Fe}] + 0.50[\text{Fe}/\text{H}], \quad (5)$$

$$[\text{Na}/\text{Fe}]_{\text{corr}} = [\text{Na}/\text{Fe}] + 0.13[\text{Fe}/\text{H}]. \quad (6)$$

Very similar slopes have been reported in the literature (see Reddy et al. 2003, Luck & Heiter 2006, and da Silva et al. 2011 in the case of C). For oxygen, we only considered the results based on the $[\text{O I}] \lambda 6300$ line (Ecuivillon et al. 2006). For Na, we assumed that the trend found by Reddy et al. (2003) extends to supersolar metallicities. No corrections are applied to the N abundances because no trend with $[\text{Fe}/\text{H}]$ is discernible for this element (Reddy et al. 2003; Ecuivillon et al. 2004b). For the thick disk star α Boo, we use the abundance offsets found by Reddy et al. (2006) between kinematically-selected samples of thin and thick disk stars (The $\Delta[\text{X}/\text{Fe}]$ values in their Table 7 were subtracted from the corrected ratios defined above.). As expected, this procedure efficiently erases the trends previously found for C and O (Fig. 11), as well as for $[\text{N}/\text{C}]$ and $[\text{N}/\text{O}]$ (not shown). Figure 12 shows that the relation between $[\text{N}/\text{Fe}]$ and $[\text{C}/\text{Fe}]$ tightens after correction and that α Boo behaves as the other red giants. To first approximation, these corrected abundances (Tables A.5 and A.6) are now free of the effects related to the nucleosynthesis history of the ISM and are, hence, more reliable probes of the mixing processes operating in our targets. As for nitrogen, note that there is no clear trend between the barium abundances (discussed below) and the metallicity (Reddy et al. 2003).

10. Discussion of some key observational results

We defer to a detailed comparison between our Li and $^{12}\text{C}/^{13}\text{C}$ abundance data and the predictions of theoretical models that incorporate rotational mixing and thermohaline instabilities to

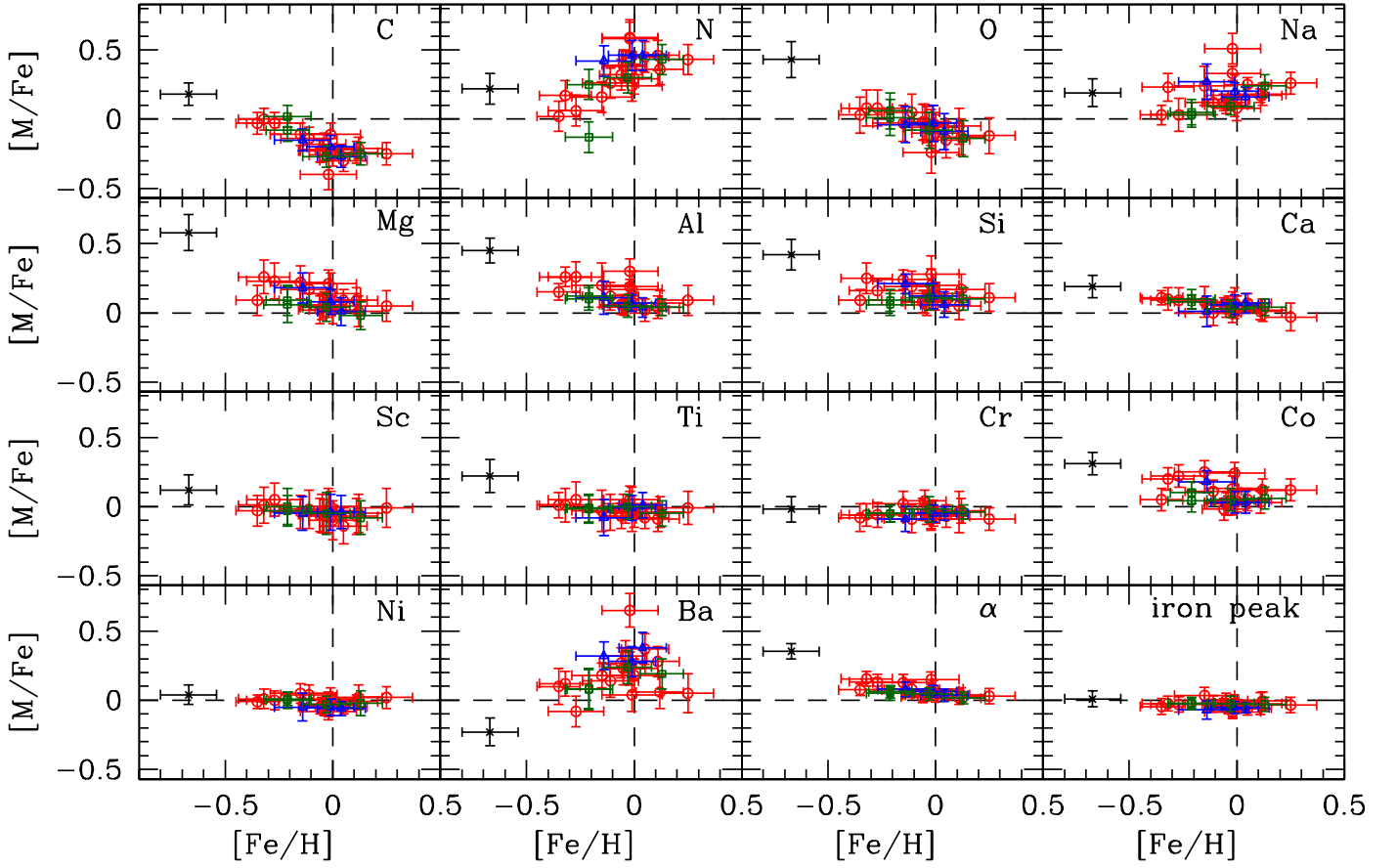


Fig. 10. Abundance ratios with respect to iron as a function of $[\text{Fe}/\text{H}]$. The results have been obtained using the spectroscopic gravities. Same symbols as in Fig. 8. The mean abundance ratio of the α -synthesised elements is defined as the unweighted mean of the Mg, Si, Ca, and Ti abundances. For the mean abundance of the iron-peak elements, we considered Cr and Ni.

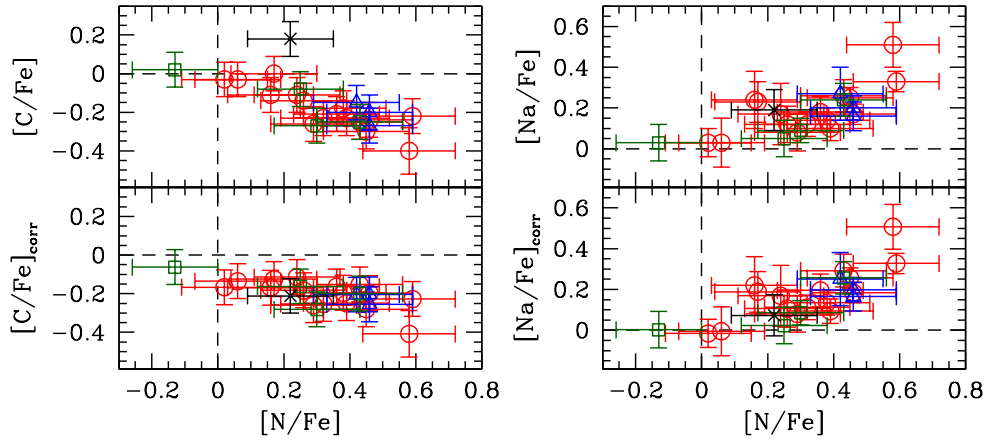


Fig. 12. Top and bottom left panels: $[\text{C}/\text{Fe}]$ as a function of $[\text{N}/\text{Fe}]$ prior and after correction for the effects of the chemical evolution of the Galaxy, respectively. Top and bottom right panels: $[\text{Na}/\text{Fe}]$ as a function of $[\text{N}/\text{Fe}]$. The results have been obtained using the spectroscopic gravities. Same symbols as in Fig. 8.

a forthcoming paper. However, let us discuss some salient results obtained for other species here. Adopting the seismic gravities leads to variations in the abundances of all elements that are comparable to the uncertainties (Tables A.4 to A.6). In the general discussion which follows, we therefore only consider the results obtained in a consistent manner for all the stars using the spectroscopic gravities. Figure 13 illustrates the complex behaviour of some key abundance ratios during the red-giant phase.

As has been known for a long time, ordinary red giants are C-poor and N-rich objects (e.g., Lambert & Ries 1981). Figure 12 shows that carbon is increasingly depleted as nitrogen is enhanced, which illustrates the differing degrees of CN-cycled material transported at the surface of our targets. This relation is quantitatively very similar for other red-giant samples (Luck & Heiter 2007; Smiljanic et al. 2009; Tautvaišienė et al. 2010, 2013) once the corrections discussed above (Sect. 9) are applied.

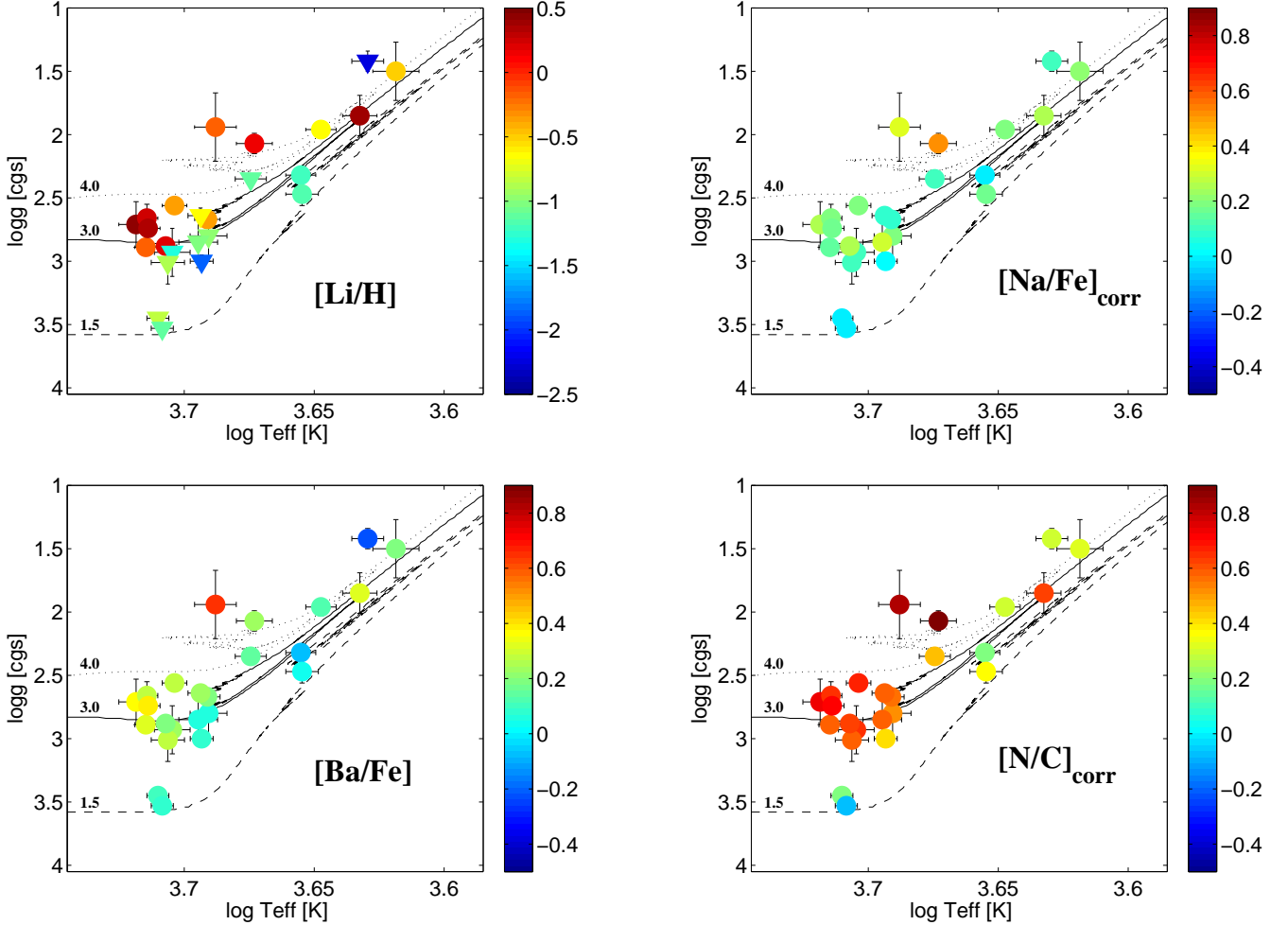


Fig. 13. Variations of some key abundance ratios across the $\log T_{\text{eff}}\text{-}\log g$ plane. For the NLTE lithium abundances, the downward-pointing triangles denote upper limits. The predictions at solar metallicity of evolutionary models for masses of 1.5, 3, and 4 M_{\odot} are overplotted for illustrative purposes. Same tracks as in Fig. 1, except that the evolutionary phase, is not colour coded.

The corrected oxygen abundances are identical within the uncertainties for all the targets (Fig. 11). There is therefore no observational evidence of ON-cycled material transported to the surface despite the detection of the products of the NeNa cycle in some stars (see below). The abundance differences indicative of an oxygen depletion might be buried in the noise.

The sodium abundance can be altered during the red-giant phase, as material processed by the NeNa cycle at temperatures in excess of $\sim 2.5 \times 10^7$ K is transported to the surface (e.g., Langer et al. 1993). However, this is only expected to occur prior to the AGB phase for intermediate-mass ($M \gtrsim 2 M_{\odot}$) stars in accordance with the solar abundance ratios found in stars with lower masses (e.g., Gratton et al. 2000). Evolutionary models predict a sodium overabundance of the order of 0.2 dex due to the first dredge-up but that can reach up to 0.8 dex for very high rotational velocities on the ZAMS (Charbonnel & Lagarde 2010). Smiljanic et al. (2009) investigated the Na abundance in giants belonging to young open clusters and found a slight increase as a function of the turn-off mass (see also Takeda et al. 2008 and Liu et al. 2010 for field giants). The largest value in our sample ($[\text{Na}/\text{Fe}]_{\text{corr}} \sim +0.5$ dex) is found for HD 50890, which is a young (155-180 Myrs) and massive (3-5 M_{\odot}) star, according to Baudin et al. (2012). Interestingly, there is also suggestive evidence that this star is spinning fast (Sect. 5.2.2). There has been

some debate in the recent literature (e.g., Smiljanic 2012, and references therein) concerning the possible existence of large (up to 0.6 dex) sodium overabundances in red giants. Although models can accommodate such high values, two results make us believe that the large excesses we observe are real. First, solar values are found for some low-mass subgiants (e.g., HD 170008 or β Aql; Fig. 1) for which no enrichment is expected. Second, there is clear evidence that the Na and N abundances increase in parallel (Fig. 12). To our knowledge, this is the first time that such a trend is so clearly uncovered (see Mishenina et al. 2006). It should be noted that the predicted NLTE corrections for Na (according to the calculations of Lind et al. 2011 and as quoted in the INSPECT database) are fairly uniform within our sample and similar to that in the Sun (about -0.1 dex). Our abundances (that are relative to solar) should hence be little affected by the neglect of NLTE effects. In the same vein, granulation effects are anticipated to have a limited impact on the strength of the Na I lines used (Collet et al. 2007).

The MgAl cycle operates above such high temperatures ($\sim 7 \times 10^7$ K; Langer et al. 1997) that Al is not expected to be produced at the expense of Mg prior to the AGB phase. The variation of the Al abundance within our sample is comparable to the uncertainties, and there is a fortiori no evidence of an Al excess accompanied by an Mg depletion when similar corrections

as described in Sect. 9 are applied using the data of Reddy et al. (2003).

It is well known that a strong barium overabundance in giant stars can result from a previous episode of mass transfer with a formerly thermally pulsing AGB (TP-AGB) companion that is now a white dwarf (Alves-Brito et al. 2011, and references therein). Barium stars are C-rich (e.g., Barbuy et al. 1992), and it is therefore very unlikely that this phenomenon plays a significant role in our sample. The Ba excess we occasionally observe may instead be attributable to a young age, as found in field dwarfs of the solar neighbourhood or members of open clusters (e.g., Bensby et al. 2007; D’Orazi et al. 2009; da Silva et al. 2012). In this respect, it may be regarded as significant that high abundances are found in the young, massive star HD 50890 and in the likely members of NGC 6633 with an estimated age in the range 450–575 Myrs according to Smiljanic et al. (2009) and van Leeuwen (2009). It is interesting to note that HD 170031 has a Ba abundance lower by about a factor 2 than these three stars, which strengthens the case for a non-membership (Sect. 2).¹⁰ The largest Ba abundance is found in the massive star HD 171427 (see Fig. 1). Once again, this can be interpreted as arising from a time evolution along the history of the Galaxy, which is of relative proportion to the yields of the various stellar populations. The combined effect of departures from LTE and time-dependent/spatial variations in the atmospheric structure due to convection is relatively small in very low-metallicity environments such as globular clusters ($\Delta[\text{Ba}/\text{Fe}] \sim 0.15$ dex compared to a 1D LTE analysis; Dobrovolskas et al. 2012), and the magnitude is likely much lower in our sample.

We conclude this discussion by a word of caution. The discrepancies between different abundance indicators discussed in Sect. 5.2.1 (see in particular Fig. 5) warn us that some effects, which are not incorporated in our analysis (e.g., departures from LTE), may bias our results, especially in the objects with the most extended and diluted atmospheres. Although we attempted to evaluate the impact for some key chemical species as far as possible and concluded that the trends observed (e.g., between $[\text{N}/\text{Fe}]$ and $[\text{Na}/\text{Fe}]$) are likely of physical origin, it should be kept in mind that these arguments rest on heterogeneous and often fragmentary calculations in the literature.

11. Concluding remarks and perspectives

We are entering a new era where spectroscopic and asteroseismic data of superb quality can be combined to provide a global view of red giants in unprecedented detail. Astrometric data from the *Gaia* space mission and new long-baseline interferometric facilities will soon also open new perspectives. On the other hand, major advances are being made on various theoretical aspects (e.g., Charbonnel & Lagarde 2010; Ludwig & Kučinskis 2012).

Our study is an effort to ultimately fully characterise the stars in our sample. This may be achieved for those for which detailed seismic information is available, such as HD 50890 (Baudin et al. 2012) or HD 181907 (Carrier et al. 2010; Miglio et al. 2010). The modelling of the CoRoT data for other stars in the seismology fields is underway (e.g., Barban et al. 2014).

The extent of mixing experienced by each of our targets results from the combined action of different physical processes

(convective and rotational mixing, as well as thermohaline instabilities) whose relative efficiency (or merely occurrence) is a complex function of their evolutionary status, mass, metallicity, and rotational history. A preliminary comparison with evolutionary models supports the widespread occurrence of mixing processes other than convection in our sample. We will take advantage of the asteroseismic constraints to provide in a forthcoming paper (Lagarde et al., in preparation) a thorough interpretation of our abundance data based on theoretical models incorporating the three mechanisms mentioned above (Charbonnel & Lagarde 2010).

Finally, dramatic advances may be expected from the analysis of the large population of red-giant stars monitored by the *Kepler* satellite. The various evolutionary sequences can clearly be distinguished from asteroseismic diagnostics (e.g., Stello et al. 2013; Montalbán et al. 2013), which opens up the possibility of mapping out the evolution of the mixing indicators during the shell-hydrogen and core-helium burning phases for a very large number of stars. An inspection of the spectra obtained by Thygesen et al. (2012) for 82 red giants in the *Kepler* field (mostly obtained with FIES installed on the Nordic Optical Telescope; NOT) shows that these data are not of sufficient quality to confidently measure the generally very weak Li and ^{13}C N features. Although demanding in terms of telescope time, such a study is amenable for the brightest targets, which can be observed on larger facilities, and may be particularly rewarding.

Acknowledgements. T.M. acknowledges financial support from Belspo for contract PRODEX GAIA-DPAC. A.M. and N.L. acknowledge fund from the Stellar Astrophysics Centre provided by The Danish National Research Foundation (Grant agreement no.: DNR106). N.L. acknowledges financial support from the Swiss National Fund. J.M. and M.V. acknowledge financial support from Belspo for contract PRODEX CoRoT. M.R. acknowledges financial support from the FP7 project *SPACEINN: Exploitation of Space Data for Innovative Helio- and Asteroseismology*. E.P. and M.L. acknowledge financial support from the PRIN-INAF 2010 (*Asteroseismology: looking inside the stars with space- and ground-based observations*). S.H. has received funding from the European Research Council under the European Communities Seventh Framework programme (FP7/2007-2013)/ERC grant agreement Stellar Ages #338251. T.K. acknowledges financial support from the Austrian Science Fund (FWF P23608). We would like to thank the referee, U. Heiter, for a careful reading of the manuscript and valuable comments. We are grateful to N. Grevesse for enlightening discussions, F. Castelli for her assistance with the interpolation of the ODF tables, K. Lind for the program to interpolate the NLTE Li corrections, as well as C. Pereira and R. Smiljanic for their help with the molecular data. This research made use of the INSPECT database (version 1.0), NASA’s Astrophysics Data System Bibliographic Services, the SIMBAD database operated at CDS, Strasbourg (France), as well as the Vienna Atomic Line Database (VALD) and the WEBDA database, both operated at the Institute for Astronomy of the University of Vienna.

References

- Abia, C., Palmerini, S., Busso, M., & Cristallo, S. 2012, *A&A*, 548, A55
- Allende Prieto, C., Barklem, P. S., Lambert, D. L., & Cunha, K. 2004, *A&A*, 420, 183
- Alonso, A., Arribas, S., & Martínez-Roger, C. 1999, *A&AS*, 140, 261
- Alves-Brito, A., Karakas, A. I., Yong, D., Meléndez, J., & Vásquez, S. 2011, *A&A*, 536, A40
- Anthony-Twarog, B. J., Deliyannis, C. P., Rich, E., & Twarog, B. A. 2013, *ApJ*, 767, L19
- Asplund, M. 2005, *ARA&A*, 43, 481
- Asplund, M., Grevesse, N., Sauval, A. J., Allende Prieto, C., & Blomme, R. 2005, *A&A*, 431, 693
- Asplund, M., Grevesse, N., Sauval, A. J., & Scott, P. 2009, *ARA&A*, 47, 481
- Baines, E. K., McAlister, H. A., Ten Brummelaar, T. A., et al. 2013, *ApJ*, 772, 16
- Barban, C., De Ridder, J., Mazumdar, A., et al. 2004, *ESASP*, 559, 113
- Barban, C., Baudin, F., Poretti, E., et al. 2014, *ASP Conf. Series*, 478, 385
- Barbuy, B., Jorissen, A., Rossi, S. C. F., & Arnould, M. 1992, *A&A*, 262, 216
- Barbuy, B., Zoccali, M., Ortolani, S., et al. 2006, *A&A*, 449, 349

¹⁰ In the context of the binary scenario mentioned above, very high precision and near-continuous radial-velocity measurements collected over about one week with SOPHIE and HARPS do not reveal the presence of a companion for the stars in NGC 6633 (Poretti et al., in preparation).

- Barklem, P. S., Piskunov, N., & O'Mara, B. J. 2000, *A&AS*, 142, 467
- Barklem, P. S., & Aspelund-Johansson, J. 2005, *A&A*, 435, 373
- Batalha, N. M., Borucki, W. J., Bryson, S. T., et al. 2011, *ApJ*, 729, 27
- Baudin, F., Barban, C., Goupil, M. J., et al. 2012, *A&A*, 538, A73
- Bauschlicher, C. W., Langhoff, S. R., & Taylor, P. R. 1988, *ApJ*, 332, 531
- Beck, P. G., Montalbán, J., Kallinger, T., et al. 2012, *Nature*, 481, 55
- Bedding, T. R., Mosser, B., Huber, D., et al. 2011, *Nature*, 471, 608
- Belkacem, K., Goupil, M. J., Dupret M. A., et al. 2011, *A&A*, 530, A142
- Bensby, T., Feltzing, S., & Lundström, I. 2003, *A&A*, 410, 527
- Bensby, T., Zenn, A. R., Oey, M. S., & Feltzing, S. 2007, *ApJ*, 663, L13
- Bergemann, M., Lind, K., Collet, R., Magic, Z., & Asplund, M. 2012, *MNRAS*, 427, 27
- Biazzo, K., Pasquini, L., Girardi, L., et al. 2007, *A&A*, 475, 981
- Borucki, W. J., Koch, D., Basri, G., et al. 2010, *Sci*, 327, 977
- Boyarchuk, M. E., Pavlenko, Y. V., & Shavrina, A. V. 1991, *Soviet Ast.*, 35, 143
- Brown, J. A., Sneden, C., Lambert, D. L., & Dutchover, Jr., E. 1989, *ApJS*, 71, 293
- Brown, T. M., Gilliland, R. L., Noyes, R. W., & Ramsey, L. W. 1991, *ApJ*, 368, 599
- Brown, J. A., & Wallerstein, G. 1992, *AJ*, 104, 1818
- Bruntt, H., Bedding, T. R., Quirion, P.-O., et al. 2010, *MNRAS*, 405, 1907
- Bruntt, H., Frandsen, S., & Thygesen, A. O. 2011, *A&A*, 528, A121
- Carlberg, J. K., Cunha, K., Smith, V. V., & Majewski, S. R. 2012, *ApJ*, 757, 109
- Carney, B. W., Gray, D. F., Yong, D., et al. 2008, *AJ*, 135, 892
- Carrier, F., De Ridder, J., Baudin, F., et al. 2010, *A&A*, 509, A73
- Carter, J. A., Agol, E., Chaplin, W. J., et al. 2012, *Science*, 337, 556
- Castelli, F., & Kurucz, R. L. 2004, in *Modelling of Stellar Atmospheres*, IAU Symp. 210 [arXiv:astro-ph/0405087]
- Chaplin, W. J., & Miglio, A. 2013, *ARA&A*, 51, 353
- Charbonnel, C., & Lagarde, N. 2010, *A&A*, 522, A10
- Chen, Y. Q., Nissen, P. E., Zhao, G., Zhang, H. W., & Benoni, T. 2000, *A&AS*, 141, 491
- Christensen-Dalsgaard, J. 2011, in *Asteroseismology*, Canary Islands Winter School of Astrophysics, Volume XXII, (editor P. L. Pallé, Cambridge University Press), arXiv:1106.5946
- Claret, A. 2000, *A&A*, 363, 1081
- Collet, R., Asplund, M., & Trampedach, R. 2007, *A&A*, 469, 687
- Cox, A. N. 2000, *Allen's Astrophysical Quantities*, 4th edn. (New York: AIP Press/Springer)
- Creevey, O. L., Doğan, G., Frasca, A., et al. 2012, *A&A*, 537, A111
- da Silva, L., Girardi, L., Pasquini, L., et al. 2006, *A&A*, 458, 609
- da Silva, R., Milone, A. C. & Reddy, B. E. 2011, *A&A*, 526, A71
- da Silva, R., Porto de Mello, G. F., Milone, A. C., et al. 2012, *A&A*, 542, A84
- Davis, S. P., Littleton, J. E., & Phillips, J. G. 1986, *ApJ*, 309, 449
- Decin, L., Vandenbussche, B., Waelkens, C., et al. 2003, *A&A*, 400, 709
- Deheuvels, S., García, R. A., Chaplin, W. J., et al. 2012, *ApJ*, 756, 19
- De Ridder, J., Barban, C., Carrier, F., et al. 2006, *A&A*, 448, 689
- De Ridder, J., Barban, C., Baudin, F., et al. 2009, *Nature*, 459, 398
- Dobrovolskas, V., Kučinskas, A., Andrievsky, S. M., et al. 2012, *A&A*, 540, A128
- Dobrovolskas, V., Kučinskas, A., Steffen, M., et al. 2013, *A&A*, 559, A102
- D'Orazi, V., Magrini, L., Randich, S., et al. 2009, *ApJ*, 693, L31
- Ecuivillon, A., Israelian, G., Santos, N. C., et al. 2004a, *A&A*, 426, 619
- Ecuivillon, A., Israelian, G., Santos, N. C., et al. 2004b, *A&A*, 418, 703
- Ecuivillon, A., Israelian, G., Santos, N. C., et al. 2006, *A&A*, 445, 633
- Fabbian, D., Asplund, M., Carlsson, M., & Kiselman, D. 2006, *A&A*, 458, 899
- Feltzing, S., & Gonzalez, G. 2001, *A&A*, 367, 253
- Fernández-Villacañas, J. L., Rego, M., & Cornide, M. 1990, *AJ*, 99, 1961
- Frandsen, S., Carrier, F., Aerts, C., et al. 2002, *A&A*, 394, L5
- Fuhrmann, K. 2004, *Astron. Nachr.*, 325, 3
- Fuhrmann, K., & Chini, R. 2012, *ApJS*, 203, 30
- Fulbright, J. P., McWilliam, A., & Rich, R. M. 2006, *ApJ*, 636, 821
- Gai, N., Basu, S., Chaplin, W. J., & Elsworth, Y. 2011, *ApJ*, 730, 63
- Gazzano, J.-C., de Laverny, P., Deleuil, M., et al. 2010, *A&A*, 523, A91
- Ghezzi, L., Cunha, K., Schuler, S. C., & Smith, V. V. 2010, *ApJ*, 725, 721
- Gilroy, K. K., & Brown, J. A. 1991, *ApJ*, 371, 578
- Girardi, L., Bressan, A., Bertelli, G., & Chiosi, C. 2000, *A&AS*, 141, 371
- Gonzalez, G., & Wallerstein, G. 1998, *AJ*, 116, 765
- Gratton, R. G., & Sneden, C. 1987, *A&A*, 178, 179
- Gratton, R. G., Sneden, C., Carretta, E., & Bragaglia, A. 2000, *A&A*, 354, 169
- Gray, D. F., & Brown, K. I. T. 2006, *PASP*, 118, 1112
- Grevesse, N., & Sauval, A. J. 1998, *Space Sci. Rev.*, 85, 161
- Griffin, R. E. M., & Lynas-Gray, A. E. 1999, *AJ*, 117, 2998
- Gustafsson, B., Edvardsson, B., Eriksson, K., et al. 2008, *A&A*, 486, 951
- Heiter, U., & Eriksson, K. 2006, *A&A*, 452, 1039
- Hekker, S., & Meléndez, J. 2007, *A&A*, 475, 1003
- Hekker, S., Broomhall, A.-M., Chaplin, W. J., et al. 2010, *MNRAS*, 402, 2049
- Hekker, S. 2013, *Advances in Space Research*, 52, 1581
- Hill, V. 1997, *A&A*, 324, 435
- Hinkle, K., Wallace, L., Valenti, J., & Harmer, D. 2000, *Visible and Near Infrared Atlas of the Arcturus Spectrum 3727-9300 Å*, (San Francisco: ASP)
- Huber, K. P., & Herzberg, G. 1979, *Constants of Diatomic Molecules*
- Huber, D., Chaplin, W. J., Christensen-Dalsgaard, J., et al. 2013, *ApJ*, 767, 127
- Jeffries, R. D., Totten, E. J., Harmer, S., & Deliyannis, C. P. 2002, *MNRAS*, 336, 1109
- Johansson, S., Litzén, U., Lundberg, H., & Zhang, Z. 2003, *ApJ*, 584, L107
- Jørgensen, U. G., & Larsson, M. 1990, *A&A*, 238, 424
- Kallinger, T., Guenther, D. B., Matthews, J. M., et al. 2008, *A&A*, 478, 497
- Kallinger, T., Mosser, B., Hekker, S., et al. 2010, *A&A*, 522, A1
- Kjeldsen, H., Bedding, T. R., Arentoft, T., et al. 2008, *ApJ*, 682, 1370
- Kovtyukh, V. V., Soubiran, C., Bienaymé, O., Mishenina, T. V., & Belik, S. I. 2006, *MNRAS*, 371, 879
- Kučinskas, A., Steffen, M., Ludwig, H.-G., et al. 2013, *A&A*, 549, A14
- Kurucz, R. L. 1990, in *Stellar Atmospheres: Beyond Classical Models*, NATO Asi Ser., eds. L. Crivellari, et al., 441
- Lacour, S., Meimon, S., Thiébaud, E., et al. 2008, *A&A*, 485, 561
- Lagarde, N., Decressin, T., Charbonnel, C., et al. 2012, *A&A*, 543, A108
- Lambert, D. L., & Ries, L. M. 1981, *ApJ*, 248, 228
- Langer, G. E., Hoffman, R. D., & Sneden, C. 1993, *PASP*, 105, 301
- Langer, G. E., Hoffman, R. D., & Zaidins, C. S. 1997, *PASP*, 109, 244
- Lecureur, N., Hill, V., Zoccali, M., et al. 2007, *A&A*, 465, 799
- Lind, K., Asplund, M., & Barklem, P. S. 2009, *A&A*, 503, 541
- Lind, K., Asplund, M., Barklem, P. S., & Belyaev, A. K. 2011, *A&A*, 528, A103
- Lind, K., Bergemann, M., & Asplund, M. 2012, *MNRAS*, 427, 50
- Liu, Y. J., Zhao, G., Shi, J. R., Pietrzyński, G., & Gieren, W. 2007, *MNRAS*, 382, 553
- Liu, Y., Sato, B., Takeda, Y., Ando, H., & Zhao, G. 2010, *PASJ*, 62, 1071
- Luck, R. E. 1977, *ApJ*, 218, 752
- Luck, R. E., & Heiter, U. 2006, *AJ*, 131, 3069
- Luck, R. E., & Heiter, U. 2007, *AJ*, 133, 2464
- Ludwig, H.-G., & Kučinskas, A. 2012, *A&A*, 547, A118
- McWilliam, A. 1990, *ApJS*, 74, 1075
- McWilliam, A., & Rich, R. M. 1994, *ApJS*, 91, 749
- Mandell, A. M., Ge, J., & Murray, N. 2004, *AJ*, 127, 1147
- Massarotti, A., Latham, D. W., Stefanik, R. P., & Fogel, J. 2008, *AJ*, 135, 209
- Matzros, E., Ryde, N., & Dupree, A. K. 2013, *A&A*, 559, A115
- Mazumdar, A., Mérand, A., Demarque, P., et al. 2009, *A&A*, 503, 521
- Meléndez, J., Barbuy, B., Bica, E., et al. 2003, *A&A*, 411, 417
- Mérand, A., Kervella, P., Barban, C., et al. 2010, *A&A*, 517, A64
- Michel, E., Baglin, A., Auvergne, M., et al. 2008, *Science*, 322, 558
- Miglio, A., Montalbán, J., Baudin, F., et al. 2009, *A&A*, 503, L21
- Miglio, A., Montalbán, J., Carrier, F., et al. 2010, *A&A*, 520, L6
- Miglio, A., Brogaard, K., Stello, D., et al. 2012, *MNRAS*, 419, 2077
- Miglio, A., Chiappini, C., Morel, T., et al. 2013, *MNRAS*, 429, 423
- Mishenina, T. V., & Kovtyukh, V. V. 2001, *A&A*, 370, 951
- Mishenina, T. V., Bienaymé, O., Gorbaneva, T. I., et al. 2006, *A&A*, 456, 1109
- Monroe, T. W. R., & Pilachowski, C. A. 2010, *AJ*, 140, 2109
- Montalbán, J., Miglio, A., Noels, A., Scuflaire, R., & Ventura, P. 2010, *ApJ*, 721, L182
- Montalbán, J., Miglio, A., Noels, A., et al. 2013, *ApJ*, 766, 118
- Morel, T., Micela, G., Favata, F., Katz, D., & Pillitteri, I. 2003, *A&A*, 412, 495
- Morel, T., Micela, G., Favata, F., & Katz, D. 2004, *A&A*, 426, 1007
- Morel, T., & Miglio, A. 2012, *MNRAS*, 419, L34
- Morel, T., Rainer, M., Poretti, E., Barban, C., & Boumier, P. 2013, *A&A*, 552, A42
- Morel, T. 2014, in *Asteroseismology of Stellar Populations in the Milky Way*, in press
- Mortier, A., Santos, N. C., Sousa, S. G., et al. 2013, *A&A*, 557, A70
- Mosser, B., & Appourchaux, T. 2009, *A&A*, 508, 877
- Mosser, B., Belkacem, K., Goupil, M. J., et al. 2010, *A&A*, 517, A22
- Mosser, B., Barban, C., Montalbán, J., et al. 2011, *A&A*, 532, A86
- Mosser, B., Goupil, M. J., Belkacem, K., et al. 2012, *A&A*, 540, A143
- Mosser, B., Michel, E., Belkacem, K., et al. 2013, *A&A*, 550, A126
- Ozel, N., Mosser, B., Dupret, M. A., et al. 2013, *A&A*, 558, A79
- Pasquini, L., Mauas, P., Käufel, H. U., & Cacciari, C. 2011, *A&A*, 531, A35
- Pavlenko, Y. V. 2008, *Astronomy Reports*, 52, 749
- Peterson, R. C., Dalle Ore, C. M., & Kurucz, R. L. 1993, *ApJ*, 404, 333
- Pilachowski, C., Sneden, C., Hinkle, K., & Joyce, R. 1997, *AJ*, 114, 819
- Plez, B. 1998, *A&A*, 337, 495
- Poretti, E., Rainer, M., Mantegazza, L., et al. 2013, *Astrophysics and Space Science Proceedings*, 31, 39
- Quirrenbach, A., Mozurkewich, D., Buscher, D. F., Hummel, C. A., & Armstrong, J. T. 1996, *A&A*, 312, 160
- Raassen, A. J. J., & Uylings, P. H. M. 1998, *A&A*, 340, 300
- Ramírez, I., & Allende Prieto, C. 2011, *ApJ*, 743, 135
- Ramírez, I., Allende Prieto, C., & Lambert, D. L. 2013, *ApJ*, 764, 78

- Recio-Blanco, A., Bijaoui, A., & de Laverny, P. 2006, MNRAS, 370, 141
- Reddy, B. E., Lambert, D. L., Hrivnak, B. J., & Bakker, E. J. 2002, AJ, 123, 1993
- Reddy, B. E., Tomkin, J., Lambert, D. L., & Allende Prieto, C. 2003, MNRAS, 340, 304
- Reddy, B. E., Lambert, D. L., & Allende Prieto, C. 2006, MNRAS, 367, 1329
- Santos, N. C., Lovis, C., Pace, G., Meléndez, J., & Naef, D. 2009, A&A, 493, 309
- Sbordone, L. 2005, Mem. S. A. It. Suppl., 8, 61
- Schuler, S. C., Hatzes, A. P., King, J. R., Kürster, M., & The, L.-S. 2006, AJ, 131, 1057
- Smiljanic, R., Gauderon, R., North, P., et al. 2009, A&A, 502, 267
- Smiljanic, R. 2012, MNRAS, 422, 1562
- Smith, V. V., Lambert, D. L., & Nissen, P. E. 1998, ApJ, 506, 405
- Smith, V. V., Suntzeff, N. B., Cunha, K., et al. 2000, AJ, 119, 1239
- Smith, V. V., Cunha, K., Shetrone, M. D., et al. 2013, ApJ, 765, 16
- Snedden, C. A. 1973, Ph.D. Thesis University of Texas, Austin
- Soubiran, C., Bienaymé, O., Mishenina, T. V., & Kovtyukh, V. V. 2008, A&A, 480, 91
- Stello, D., Bruntt, H., Preston, H., & Buzasi, D. 2008, ApJ, 674, L53
- Stello, D., Huber, D., Bedding, T. R., et al. 2013, ApJ, 765, L41
- Takeda, Y., Sato, B., & Murata, D. 2008, PASJ, 60, 781
- Tarrant, N. J., Chaplin, W. J., Elsworth, Y., Sreckley, S. A., & Stevens, I. R. 2007, MNRAS, 382, L48
- Tassoul, M. 1980, ApJS, 43, 469
- Tautvaišienė, G., Edvardsson, B., Puzeras, E., Barisevičius, G., & Ilyin, I. 2010, MNRAS, 409, 1213
- Tautvaišienė, G., Barisevičius, G., Chorniy, Y., Ilyin, I., & Puzeras, E. 2013, MNRAS, 430, 621
- Thorén, P., Edvardsson, B., & Gustafsson, B. 2004, A&A, 425, 187
- Thygesen, A. O., Frandsen, S., Bruntt, H., et al. 2012, A&A, 543, A160
- Tomkin, J., Lambert, D. L., & Luck, R. E. 1975, ApJ, 199, 436
- Tomkin, J., & Lambert, D. L. 1999, ApJ, 523, 234
- Torres, G., Fischer, D. A., Sozzetti, A., et al. 2012, ApJ, 757, 161
- Unsöld, A. 1955, Physik der Sternatmosphären, MIT besonderer Berücksichtigung der Sonne (Berlin: Springer)
- Valenti, J. A., & Fischer, D. A. 2005, ApJS, 159, 141
- Valentini, M., Morel, T., Miglio, A., Fossati, L., & Munari, U. 2013, EPJ Web of Conferences, 43, 03006
- van Leeuwen, F. 2007, Hipparcos, the new reduction of the raw data (Dordrecht: Springer)
- van Leeuwen, F. 2009, A&A, 497, 209
- White, T. R., Bedding, T. R., Stello, D., et al. 2011, ApJ, 743, 161
- Wyller, A. A. 1966, ApJ, 143, 828
- Zhao, G., Qiu, H. M., & Mao, S. 2001, ApJ, 551, L85
- Zoccali, M., Barbuy, B., Hill, V., et al. 2004, A&A, 423, 507

Appendix A: Literature results for the benchmark stars.

Table A.1 provides the literature data for the benchmark stars.

Table A.1. Atmospheric parameters, iron content, and abundances of mixing indicators found in the literature for the benchmark stars.

Star	T_{eff} [K]		$\log g$ [cgs]		ξ [km s $^{-1}$]	[Fe/H]	[Li/H] LTE	[C/Fe]	[N/Fe]	[O/Fe]	[Na/Fe]	Ref.
	Value	Method	Value	Method								
α Boo	4255	E	1.45	I	1.77	-0.67	<-2.50	+0.18	+0.22	+0.43	+0.19	
	4260	E	[1.42]	A	1.77	-0.69	<-2.45	+0.19	+0.22	+0.44	+0.21	
	4400	E	2.0	I	1.5	-0.51	+0.18	1
	4250	E	1.3	I	1.7	-0.68	...	+0.00	+0.28	+0.45	+0.20	2
	4300	E	1.5	I	1.7	-0.63	3
	4300	E	1.7	I	1.6	-0.72	+0.42	+0.32	4
	4350	E	1.6	I	1.6	-0.58	5
	4275	E	1.5	I	1.6	-0.58	6 ^a
	4300	E	1.8	I	1.6	-0.57	+0.05	7
	4368	E	1.86	I	1.86	-0.62	8
	4330	P	1.5	I	1.5	-0.38	9
	4340	P	1.9	LMT	...	-0.37	<-1.89	10
	4300	P	2.0	P	1.5	-0.69	11
	4330	P	2.1	LMT	1.6	-0.58	-0.10	12
	4300	S	1.5	S	1.7	-0.5	...	+0.04	+0.43	+0.50	+0.30	13
	4280	P	1.3	I	1.4	-0.54	<-1.91	+0.10	14
	4292	F	1.94	F	...	-0.51	15
	4320	F	1.50	F	1.7	-0.5	...	-0.06	+0.19	+0.35	...	16
	4275	P	1.55	LMT	1.65	-0.54	...	-0.05	+0.35	+0.47	...	17
	4277	S	1.7	S	...	-0.47	18
	4300	E	1.50	LMT	1.5	-0.49	+0.04	19
	4286	F	1.66	LMT	1.74	-0.52	...	+0.43	...	+0.50	+0.11	20
	4215	E	1.53	LMT	1.65	-0.60	+0.67 ^b	...	21
4275	P	1.7	LMT	1.85	-0.52	...	-0.04	+0.24	+0.33	...	22	
4244	E	1.55	LMT	1.61	-0.55	23	
η Ser	4915	E	3.07	I	1.14	-0.21	<-2.00	-0.08	+0.25	+0.06	+0.05	
	4935	E	[3.00]	A	1.17	-0.24	<-1.90	-0.07	+0.28	+0.06	+0.10	
	4850	E	2.96	I	1.04	-0.11	-0.91	-0.18	-0.05	24
	4972	E	3.12	I	1.17	-0.18	...	-0.03	+0.05	25 ^c
	4955	E	3.20	I	1.33	-0.15	26
	4944	E	3.12	I	1.25	-0.17	27
	4890	P	3.21	LMT	2.1	-0.25	28
	4809	LDR	29
	4975	S	3.29	S	0.85	-0.05	-0.05	30
	4917	B	3.06	I	1.14	-0.20	31
	4936	P	3.04	LMT	1.1	-0.27	32
	ϵ Oph	4935	E	2.66	I	1.42	-0.03	<-0.80	-0.27	+0.30	-0.08	+0.09
4940		E	[2.64]	A	1.43	-0.04	<-0.80	-0.26	+0.31	-0.08	+0.10	
4931		E	2.69	I	1.34	-0.07	...	-0.27	+0.05	25 ^c
4970		E	2.90	I	1.52	-0.07	26
5021		E	3.02	I	1.54	-0.01	<-1.26	-0.28	+0.38	+0.06	+0.07	33
4850		P	3.03	LMT	2.2	-0.08	28
4861		P	2.77	LMT	1.4	-0.08	-0.01 ^b	+0.12	34
ξ Hya	5080	E	2.96	I	1.32	+0.13	+0.07	-0.25	+0.43	-0.14	+0.24	
	5095	E	[2.88]	A	1.34	+0.10	+0.09	-0.24	+0.47	-0.15	+0.28	
	5045	E	2.76	I	1.20	+0.21	+0.39	-0.45	...	-0.02	+0.23	24
	4996	E	2.53	LMT	1.39	+0.08	23
	5010	P	2.93	LMT	2.1	+0.13	28
β Aql	5100	E	3.56	I	0.97	-0.21	<-1.20	+0.02	-0.13	+0.01	+0.03	
	5110	E	[3.53]	A	0.99	-0.22	<-1.15	+0.02	-0.12	+0.00	+0.04	
	5030	E	3.49	I	0.88	-0.21	-0.73	-0.09	+0.03	24
	5160	E	3.68	I	0.92	-0.12	<-0.47	-0.04	...	+0.06	...	35
	5062	E	3.54	LMT	0.97	-0.19	+0.13 ^b	...	21
	5100	P	3.60	LMT	1.8	-0.13	28
	5163	S	3.79	S	0.85	-0.10	-0.05	30
	5111	P	3.52	LMT	1.2	-0.28	32
	5106	P	3.54	LMT	1.15	-0.15	...	-0.23	...	-0.03	...	36
	5110	B	3.60	I	0.92	-0.17	37

Notes. The rows in boldface show the results of this study, either using the spectroscopic or the seismic $\log g$ (given in square brackets). The abundances were rescaled to our adopted solar values when appropriate and whenever these were not quoted in the original paper. **E**: from excitation equilibrium of the Fe I lines; **I**: from ionisation equilibrium of Fe; **P**: from photometric data; **LMT**: from estimates of the luminosity, mass, and effective temperature; **S**: from spectral synthesis; **F**: from fitting of the spectral energy distribution; **LDR**: from line-depth ratios; **B**: from fitting the Balmer line wings; **A**: from asteroseismology. References. (1) Hill 1997; (2) Gonzalez & Wallerstein 1998; (3) Tomkin & Lambert 1999; (4) Smith et al. 2000; (5) Mishenina & Kovtyukh 2001; (6) Reddy et al. 2002; (7) Zoccali et al. 2004; (8) Mortier et al. 2013 (using Kurucz models and the 'TS13' line list); (9) Gratton & Sneden 1987; (10) Brown et al. 1989; (11) Fernández-Villacañas et al. 1990; (12) Brown & Wallerstein 1992; (13) Peterson et al. 1993; (14) McWilliam & Rich 1994; (15) Griffin & Lynas-Gray 1999; (16) Decin et al. 2003; (17) Meléndez et al. 2003; (18) Recio-Blanco et al. 2006; (19) Lecureur et al. 2007; (20) Ramírez & Allende Prieto 2011; (21) Ramírez et al. 2013; (22) Smith et al. 2013; (23) Fulbright et al. 2006; (24) Bruntt et al. 2010; (25) Takeda et al. 2008; (26) Hekker & Meléndez 2007; (27) Ghezzi et al. 2010; (28) McWilliam 1990; (29) Kovtyukh et al. 2006; (30) Valenti & Fischer 2005; (31) Fuhrmann & Chini 2012; (32) Matrozis et al. 2013; (33) Luck & Heiter 2007; (34) Liu et al. 2007; (35) Luck & Heiter 2006; (36) Allende Prieto et al. 2004; (37) Fuhrmann 2004. ^(a) Also based on Hinkle et al. (2000) atlas. ^(b) NLTE value. ^(c) As Takeda et al. caution, their oxygen abundances may not be reliable.

Table A.2. EW measurements (the full table is available in electronic form). Only values eventually retained for the analysis are listed.

Line	EW [mÅ]														
	HD 40726	HD 42911	HD 43023	HD 45398	HD 49429	HD 49566	HD 50890	HD 169370	HD 169751	HD 170008	HD 170031	HD 171427	HD 175294	HD 175679	HD 178
Fe I λ 5543.937	91.2	95.5	83.3	101.2	82.2	81.7	110.6	84.7	83.4	63.6	96.7	118.9	105.8	92.1	9
Fe I λ 5638.262	109.0	114.5	101.2	...	96.7	96.6	134.3	104.8	100.3	75.0	...	141.9	124.3	112.2	11
Fe I λ 5679.025	81.2	87.7	76.2	85.3	74.9	72.9	102.5	73.8	77.2	55.9	86.6	100.9	96.0	84.9	11
Fe I λ 5732.275	29.3	40.0	41.3	51.0	...	3
Fe I λ 5775.080	87.6	94.7	82.8	99.6	78.6	78.6	108.6	83.9	85.8	61.1	95.8	117.7	105.9	92.1	9
Fe I λ 5806.717	80.9	88.9	74.1	88.5	73.6	71.8	108.1	76.1	78.0	52.6	87.6	100.9	101.0	82.9	8
Fe I λ 5848.123	...	86.1	70.2	100.3	76.8	76.3	...	93.7	...	93.7	...	8
Fe I λ 5855.091	40.3	51.2	38.4	53.5	36.9	37.0	51.5	40.2	42.4	23.1	51.6	51.8	55.6	44.1	4
Fe I λ 5902.473	...	37.5	24.8	29.6	...	13.9	41.4	33.6	3
Fe I λ 5905.689	79.8	86.8	74.0	...	74.1	72.1	102.8	55.1	87.0	84.6	8
Fe I λ 5909.970	83.3	74.4	119.1	99.4
Fe I λ 5916.247	...	110.1	93.2	132.8	91.4	90.1	...	109.6	98.7	...	119.5	147.0	128.1	109.7	11
Fe I λ 5927.786	65.1	71.0	...	74.1	...	58.2	...	60.8	63.9	42.1	73.2	80.7	73.2	...	6
Fe I λ 5929.667	64.2	71.2	61.2	73.1	56.5	57.3	84.1	61.3	64.1	40.2	72.2	83.6	...	66.1	6
Fe I λ 5930.173	112.9	115.9	105.4	114.5	101.3	100.3	136.4	100.8	106.1	81.4	116.4	143.6	130.4	116.5	10
Fe I λ 5947.503	19.2	10.3	34.2	26.9	2
Fe I λ 6027.050	102.2	101.8	89.6	106.3	87.0	85.9	132.0	90.8	89.9	66.0	101.5	132.7	114.1	102.3	9
Fe I λ 6078.491	101.1	104.4	91.9	102.5	89.8	89.2	123.7	89.9	94.3	71.4	103.8	128.7	114.9	101.7	9
Fe I λ 6078.999	69.8	75.3	64.3	75.6	62.1	61.7	94.0	64.3	67.1	45.8	75.9	91.9	83.9	72.3	6
Fe I λ 6093.644	51.1	61.2	49.5	62.3	47.0	46.1	74.3	51.4	52.0	31.5	62.5	69.1	68.1	55.0	5
Fe I λ 6094.364	35.1	47.1	34.7	49.7	32.6	32.2	62.2	38.9	39.6	21.0	49.1	51.3	55.8	40.4	4
Fe I λ 6096.665	64.2	75.6	62.0	80.5	59.3	59.0	96.0	67.0	67.5	41.2	78.5	86.9	82.7	71.2	7
Fe I λ 6098.280	36.7	45.1	34.1	52.2	33.2	30.8	...	37.1	38.6	18.6	48.9	...	55.0	41.7	4
Fe I λ 6120.249	28.2	49.4	31.6	90.7	28.6	25.1	74.5	57.8	42.4	15.6	67.4	57.8	54.1	32.8	6
Fe I λ 6151.617	91.5	104.0	89.5	135.4	85.5	84.0	134.0	103.7	94.8	64.2	115.3	136.7	112.4	95.5	11
Fe I λ 6165.361	73.6	81.1	67.9	87.5	67.1	66.0	104.1	72.0	72.9	47.6	84.1	98.3	88.6	76.4	7
Fe I λ 6187.987	78.6	90.2	74.2	96.1	71.2	70.6	100.5	78.7	79.3	51.2	91.2	107.7	96.9	83.8	8
Fe I λ 6219.279	141.8	155.2	132.7	...	128.9	128.1	191.5	149.1	141.7	100.4	170.5	207.9	170.3	148.9	16
Fe I λ 6240.646	91.2	106.2	88.9	130.7	84.6	83.3	...	101.4	96.6	62.6	114.4	139.4	114.2	97.0	11
Fe I λ 6252.554	167.6	188.9	162.9	...	156.8	...	215.0	186.7	...	129.6	207.2	...	201.8	174.7	11
Fe I λ 6322.690	120.0	134.7	...	158.2	110.1	108.8	169.7	127.2	122.1	85.9	143.4	176.6	145.2	122.2	14
Fe I λ 6335.328	147.8	165.3	142.7	...	137.9	137.4	...	163.3	149.1	108.5	182.4	153.8	14
Fe I λ 6336.823	137.0	...	125.6	150.2	122.3	122.8	...	131.1	128.0	100.6	149.9	189.0	165.9	139.3	14
Fe I λ 6436.411	...	39.6	25.7	45.8	22.5	23.7	...	29.0	30.7	11.6	42.0	42.8	47.2	32.5	...
Fe I λ 6469.213	118.6
Fe I λ 6498.939	105.9	122.9	101.8	...	97.6	92.5	166.6	126.5	110.6	69.7	142.0	164.9	134.1	110.8	14
Fe I λ 6574.228	82.1	103.2	82.7	147.8	...	73.3	...	107.5	91.6	53.0	120.5	130.9	115.8	88.9	12
Fe I λ 6593.871	137.2	152.7	127.7	179.3	144.9	138.4	...	161.2	199.6	167.6	145.0	15
Fe I λ 6699.162	...	30.4	18.2	32.9	19.0	16.7	...	21.3	27.0	...	32.6	38.6	36.4	23.7	2
Fe I λ 6703.567	76.2	88.8	73.0	105.8	70.1	68.6	...	82.6	78.5	48.5	95.2	112.0	96.9	82.9	9
Fe I λ 6713.771	39.1	49.2	36.7	49.1	37.5	41.5	20.6	50.0	53.0	58.7	43.2	4
Fe I λ 6725.353	36.4	49.1	36.0	53.6	35.6	33.0	62.9	41.5	42.6	21.1	52.6	50.8	56.1	42.9	4
Fe I λ 6726.661	67.4	78.0	65.8	78.5	63.8	62.3	96.2	67.1	69.8	45.8	78.6	88.4	88.3	73.8	7
Fe I λ 6733.151	48.8	60.6	46.0	61.1	43.9	43.3	72.3	47.4	51.6	27.6	60.3	67.2	67.3	55.0	5
Fe I λ 6745.090	...	29.9	20.0	32.7	19.4	17.6	...	22.2	24.6	...	31.6	34.3	37.2	...	2
Fe I λ 6750.150	122.7	136.7	114.3	160.1	...	110.8	...	128.0	123.3	86.5	146.1	180.0	151.9	130.9	14
Fe I λ 6806.847	74.6	88.3	71.7	107.3	67.6	66.1	119.1	82.1	79.1	47.2	95.4	112.4	100.9	80.7	7
Fe I λ 6810.257	73.7	82.8	70.0	84.0	66.7	67.2	103.6	68.6	73.2	49.0	83.6	96.3	91.9	77.7	7
Fe I λ 6820.369	66.8	79.1	61.9	...	61.2	59.4	94.6	65.7	68.7	41.2	80.9	89.4	86.1	70.6	7
Fe I λ 6843.648	89.5	97.8	80.9	96.9	80.3	80.2	114.4	84.8	89.0	60.3	97.5	118.2	108.8	91.1	7
Fe I λ 6857.243	45.4	58.5	42.7	63.4	43.5	40.9	65.5	48.1	48.7	24.8	59.8	61.6	62.4	48.9	5
Fe I λ 6862.492	55.4	66.3	49.0	67.2	51.0	49.1	75.4	51.6	55.9	31.3	64.7	76.2	...	68.2	5
Fe I λ 6988.523
Fe I λ 7022.953
Fe I λ 7219.678
Fe I λ 7306.556
Fe I λ 7547.896	55.4	43.2	...
Fe I λ 7723.208	119.7	95.8	...
Fe I λ 7746.587	58.4
Fe I λ 7748.274
Fe I λ 7751.137	95.1	78.2	...
Fe I λ 7780.552	164.9	146.4	...
Fe I λ 7802.473	44.9	31.6	...
Fe I λ 7807.952	105.9	93.5	...
Fe I λ 8239.127
Fe I λ 8922.643
Fe II λ 5264.812	...	68.8	66.2	55.1	65.9	67.1	...	50.4	62.1	43.8	59.2	104.2	77.3	76.3	5
Fe II λ 5425.257	76.4	62.2	58.2	50.4	58.2	59.2	...	45.2	56.8	37.7	52.6	97.8	70.1	71.9	5
Fe II λ 5991.376	68.5	...	50.1	52.3	49.4	29.0	...	90.2	4
Fe II λ 6149.258	70.6	54.6	49.2	...	49.6	51.8	...	34.8	47.3	32.2	42.7	86.8	63.0	62.0	4
Fe II λ 6247.557	92.4	70.3	67.6	45.8	65.4	69.4	94.7	46.2	64.4	45.9	52.7	112.4	76.8	80.5	5
Fe II λ 6369.462	49.9	40.8	34.8	31.2	35.2	36.9	57.1	24.8	36.0	18.2	32.1	67.3	...	43.3	3
Fe II λ 6416.919	74.1	...	52.8	...	52.1	54.8	80.6	...	53.8	34.1	...	84.8	65.4	63.6	3
Fe II λ 6432.680	...	67.2	60.3	50.5	60.8	47.0	60.3	38.5	...	101.4	74.6	76.8	...
Fe II λ 6456.383	104.6	80.1	78.2	55.2	...	81.6	...	55.7	75.1	54.0	62.8	130.5	93.1	92.2	6
Fe II λ 7711.723	77.1	...
O I λ 7771.944	60.1	70.4	...
O I λ 7774.166	56.7	59.4	...
O I λ 7775.388	51.5	45.8	...
Na I λ 6154.226	76.7	89.9	63.9	111.3	63.2	63.0	129.4	70.5	70.9	37.3	97.8	106.8	108.8	79.3	8
Na I λ 6160.747	97.6	111.5	86.3	134.0	85.4	84.0	138.7	93.4	94.2	57.8	121.4	127.9	125.3	99.9	10
Mg I λ 5711.088	130.4	139.7	122.7	153.7	119.8	120.8	163.7	138.7	127.0	104.5	150.4	156.3	155.4	138.3	14
Al I λ 6696.023	...	78.3	59.4	106.5	57.6	54.2	...	82.8	67.4	43.1	94.7	87.1	92.8	68.9	8
Al I λ 6698.673	38.2	55.2	37.7	78.4											

Table A.3. Line list and atomic data.

Ion	λ [Å]	LEP [eV]	$\log gf$	$\log C_6$	$E_\gamma^{5/2}$	Ion	λ [Å]	LEP [eV]	$\log gf$	$\log C_6$	$E_\gamma^{5/2}$
Fe I	5543.937	4.218	-1.089	-30.523	...	Fe I	7746.587	5.064	-1.330	...	3.07
Fe I	5638.262	4.221	-0.841	-30.541	...	Fe I	7748.274	2.949	-1.816	-31.321	...
Fe I	5679.025	4.652	-0.802	-30.090	...	Fe I	7751.137	4.992	-0.799	...	3.07
Fe I	5732.275	4.992	-1.233	-30.731	...	Fe I	7780.552	4.474	-0.154	...	3.07
Fe I	5775.080	4.221	-1.141	...	3.07	Fe I	7802.473	5.086	-1.297	...	3.07
Fe I	5806.717	4.608	-0.913	-30.216	...	Fe I	7807.952	4.992	-0.527	...	3.07
Fe I	5848.123	4.608	-0.900	...	3.07	Fe I	8239.127	2.424	-3.306	...	3.07
Fe I	5855.091	4.608	-1.612	-30.241	...	Fe I	8922.643	4.992	-1.442	...	3.07
Fe I	5902.473	4.593	-1.806	-31.809	...	Fe II	5264.812	3.231	-3.093	...	3.07
Fe I	5905.689	4.652	-0.792	-30.206	...	Fe II	5425.257	3.200	-3.271	...	3.07
Fe I	5909.970	3.211	-2.551	-30.562	...	Fe II	5991.376	3.153	-3.595	-32.110	...
Fe I	5916.247	2.454	-2.923	-31.367	...	Fe II	6149.258	3.889	-2.782	-32.025	...
Fe I	5927.786	4.652	-1.121	-30.217	...	Fe II	6247.557	3.892	-2.367	-32.025	...
Fe I	5929.667	4.549	-1.251	-30.358	...	Fe II	6369.462	2.891	-4.169	-32.129	...
Fe I	5930.173	4.652	-0.356	-30.218	...	Fe II	6416.919	3.892	-2.738	-32.031	...
Fe I	5947.503	4.607	-1.928	...	3.07	Fe II	6432.680	2.891	-3.606	-32.129	...
Fe I	6027.050	4.076	-1.166	...	3.07	Fe II	6456.383	3.904	-2.185	-32.031	...
Fe I	6078.491	4.796	-0.388	...	3.07	Fe II	7711.723	3.904	-2.555	-32.031	...
Fe I	6078.999	4.652	-1.050	-30.290	...	O I	7771.944	9.147	0.339	-31.059	...
Fe I	6093.644	4.608	-1.378	-30.356	...	O I	7774.166	9.147	0.169	-31.059	...
Fe I	6094.364	4.652	-1.622	-30.297	...	O I	7775.388	9.147	-0.065	-31.059	...
Fe I	6096.665	3.984	-1.855	-30.240	...	Na I	6154.226	2.102	-1.581	...	5.20
Fe I	6098.280	4.559	-1.777	-30.446	...	Na I	6160.747	2.105	-1.323	...	5.20
Fe I	6120.249	0.915	-5.950	...	3.07	Mg I	5711.088	4.346	-1.852	...	9.88
Fe I	6151.617	2.176	-3.350	-31.593	...	Al I	6696.023	3.143	-1.612	...	9.88
Fe I	6165.361	4.143	-1.522	...	3.07	Al I	6698.673	3.143	-1.878	...	9.88
Fe I	6187.987	3.944	-1.688	-30.310	...	Al I	7835.309	4.022	-0.731	...	9.88
Fe I	6219.279	2.198	-2.468	-31.589	...	Si I	5793.073	4.930	-1.947	...	1.93
Fe I	6240.646	2.223	-3.376	-31.503	...	Si I	5948.541	5.083	-1.243	-29.660 ^a	...
Fe I	6252.554	2.404	-1.891	-31.416	...	Si I	6029.869	5.984	-1.581	...	1.93
Fe I	6322.690	2.588	-2.435	-31.355	...	Si I	6155.134	5.620	-0.840	...	1.93
Fe I	6335.328	2.198	-2.427	-31.601	...	Si I	6721.848	5.863	-1.147	...	1.93
Fe I	6336.823	3.687	-1.049	-30.382	...	Si I	7034.901	5.871	-0.829	...	1.93
Fe I	6436.411	4.187	-2.380	...	3.07	Si I	7680.266	5.863	-0.697	...	1.93
Fe I	6469.213	4.835	-0.616	-30.219	...	Si I	7760.628	6.206	-1.354	...	1.93
Fe I	6498.939	0.958	-4.662	-31.814	...	Si I	8742.446	5.871	-0.531	...	1.93
Fe I	6574.228	0.990	-5.011	...	3.07	Si I	8892.720	5.984	-0.689	...	1.93
Fe I	6593.871	2.433	-2.296	-31.433	...	Ca I	6166.439	2.521	-1.196	-30.226	...
Fe I	6699.162	4.593	-2.059	-31.517	...	Ca I	6455.598	2.523	-1.383	-31.293	...
Fe I	6703.567	2.759	-3.080	-31.436	...	Ca I	6499.650	2.523	-0.866	-31.296	...
Fe I	6713.771	4.796	-1.540	-30.367	...	Sc II	6320.851	1.500	-1.826	...	6.91
Fe I	6725.353	4.104	-2.221	-30.317	...	Ti I	5766.330	3.294	0.345	...	4.98
Fe I	6726.661	4.607	-1.132	...	3.07	Cr I	5787.965	3.323	-0.210	-30.099	...
Fe I	6733.151	4.639	-1.454	-30.468	...	Cr I	6882.475	3.438	-0.293	-30.382	...
Fe I	6745.090	4.580	-2.058	-31.679	...	Cr I	6882.996	3.438	-0.355	-30.382	...
Fe I	6750.150	2.424	-2.610	-31.387	...	Cr I	6925.202	3.450	-0.282	-30.382	...
Fe I	6806.847	2.728	-3.140	-31.460	...	Co I	6454.990	3.632	-0.262	-30.423	...
Fe I	6810.257	4.607	-1.035	-30.347	...	Ni I	5593.733	3.899	-0.823	-30.403	...
Fe I	6820.369	4.639	-1.199	-30.311	...	Ni I	5805.213	4.168	-0.572	-30.387	...
Fe I	6843.648	4.549	-0.891	-30.532	...	Ni I	6111.066	4.088	-0.873	-30.382	...
Fe I	6857.243	4.076	-2.052	...	3.07	Ni I	6176.807	4.088	-0.287	-30.407	...
Fe I	6862.492	4.559	-1.392	-30.436	...	Ni I	6186.709	4.106	-0.882	-30.392	...
Fe I	6988.523	2.404	-3.485	-31.467	...	Ni I	6204.600	4.088	-1.128	-30.557	...
Fe I	7022.953	4.191	-1.183	-30.299	...	Ni I	6223.981	4.106	-0.909	-30.405	...
Fe I	7219.678	4.076	-1.607	...	3.07	Ni I	6772.313	3.658	-0.983	-30.448	...
Fe I	7306.556	4.178	-1.574	...	3.07	Ni I	7555.598	3.848	-0.109	...	4.04
Fe I	7547.896	5.100	-1.158	...	3.07	Ni I	7797.586	3.899	-0.292	...	4.04
Fe I	7723.208	2.279	-3.500	-31.492	...	Ba II	5853.668	0.604	-0.921	-31.293	...

Notes. Wavelength of the transition, lower excitation potential, calibrated oscillator strength, interaction constant for van der Waals interaction, C_6 , or empirical enhancement factor to the line width parameter, E_γ , when the latter is not available. The interaction constants were derived from the line broadening cross sections computed by Barklem et al. (2000) and Barklem & Aspelund-Johansson (2005). ^(a) From Barbuy et al. (2006).

Table A.4. Abundance data with $1\text{-}\sigma$ uncertainties.

	[Mg/Fe]	[Al/Fe]	[Si/Fe]	[Ca/Fe]	[Sc/Fe]	[Ti/Fe]	[Cr/Fe]	[Co/Fe]	[Ni/Fe]	[Ba/Fe]
Sun	7.58	6.47	7.55	6.36	3.17	5.02	5.67	4.92	6.25	2.13
HD 40726	0.09±0.08	0.02±0.08	0.09±0.08	0.07±0.07	-0.14±0.13	-0.08±0.08	-0.07±0.08	0.05±0.08	-0.05±0.05	0.37±0.11
HD 42911	0.01±0.11	0.07±0.09	0.17±0.11	0.02±0.08	-0.05±0.14	-0.04±0.11	-0.03±0.09	0.12±0.08	0.02±0.09	0.06±0.12
HD 43023	0.04±0.09	0.06±0.07	0.08±0.08	0.03±0.06	-0.05±0.14	0.00±0.09	0.04±0.08	0.02±0.08	-0.04±0.06	0.23±0.12
HD 45398	0.22±0.12	0.20±0.16	0.24±0.07	0.08±0.11	-0.04±0.12	-0.03±0.15	0.02±0.09	0.25±0.08	0.05±0.07	0.18±0.09
HD 49429	0.02±0.10	0.06±0.07	0.08±0.08	0.06±0.05	-0.06±0.12	-0.07±0.09	-0.02±0.08	-0.02±0.08	-0.05±0.05	0.27±0.11
HD 49566	0.06±0.09	0.04±0.06	0.06±0.08	0.07±0.05	-0.07±0.12	-0.04±0.08	-0.05±0.08	0.02±0.08	-0.05±0.06	0.32±0.11
	0.12±0.08	0.09±0.06	0.09±0.06	0.12±0.05	-0.09±0.08	0.01±0.08	0.00±0.08	0.06±0.08	-0.02±0.06	0.31±0.10
HD 50890	0.21±0.10	0.30±0.09	0.28±0.13	0.06±0.09	...	0.05±0.10	-0.09±0.08	0.13±0.09	-0.03±0.09	0.23±0.12
	0.10±0.08	0.20±0.09	0.25±0.13	-0.04±0.09	...	-0.05±0.10	-0.19±0.08	0.07±0.08	-0.08±0.09	0.23±0.10
HD 169370	0.23±0.13	0.26±0.11	0.16±0.07	0.09±0.09	0.05±0.12	0.05±0.13	-0.06±0.09	0.22±0.08	0.00±0.07	-0.08±0.11
	0.22±0.08	0.25±0.09	0.15±0.05	0.08±0.06	0.05±0.08	0.04±0.10	-0.07±0.07	0.22±0.08	-0.01±0.07	-0.09±0.09
HD 169751	0.02±0.10	0.07±0.07	0.12±0.10	0.05±0.07	-0.10±0.14	-0.05±0.10	-0.06±0.06	0.04±0.08	-0.03±0.08	0.18±0.12
	0.05±0.08	0.09±0.05	0.13±0.09	0.08±0.06	-0.10±0.09	-0.02±0.09	-0.03±0.05	0.05±0.08	-0.01±0.08	0.18±0.10
HD 170008	0.09±0.11	0.15±0.06	0.09±0.08	0.11±0.05	-0.03±0.11	-0.01±0.09	-0.08±0.10	0.05±0.08	-0.01±0.05	0.10±0.13
	0.08±0.08	0.14±0.06	0.08±0.06	0.10±0.05	-0.03±0.08	0.00±0.09	-0.09±0.08	0.04±0.08	-0.01±0.05	0.10±0.10
HD 170031	0.14±0.15	0.17±0.13	0.14±0.05	0.07±0.11	0.00±0.11	-0.02±0.16	-0.05±0.09	0.24±0.08	0.01±0.08	0.04±0.12
	0.08±0.09	0.11±0.10	0.12±0.05	0.02±0.08	-0.02±0.08	-0.09±0.13	-0.11±0.07	0.21±0.08	-0.02±0.08	0.03±0.09
HD 171427	0.05±0.08	0.19±0.05	0.20±0.12	0.01±0.08	-0.03±0.16	0.02±0.09	-0.09±0.07	0.03±0.09	-0.08±0.06	0.65±0.12
HD 175294	0.05±0.11	0.09±0.11	0.11±0.10	-0.03±0.10	-0.01±0.14	-0.01±0.12	-0.09±0.08	0.12±0.08	0.02±0.08	0.05±0.14
HD 175679	0.09±0.09	0.04±0.08	0.05±0.10	0.01±0.06	-0.07±0.13	-0.09±0.09	-0.04±0.15	0.03±0.08	-0.01±0.05	0.28±0.11
	0.23±0.08	0.16±0.07	0.11±0.10	0.12±0.05	-0.11±0.10	0.03±0.08	0.07±0.15	0.11±0.08	0.05±0.05	0.25±0.10
HD 178484	0.26±0.12	0.26±0.07	0.25±0.11	0.10±0.08	0.01±0.13	0.01±0.12	-0.06±0.08	0.20±0.08	0.01±0.07	0.12±0.09
	0.22±0.09	0.22±0.07	0.24±0.11	0.06±0.07	0.01±0.09	-0.03±0.12	-0.10±0.08	0.18±0.08	0.00±0.07	0.11±0.09
HD 181907	0.17±0.12	0.12±0.10	0.19±0.11	0.00±0.09	-0.02±0.14	-0.04±0.13	-0.09±0.10	0.11±0.08	0.04±0.07	0.14±0.12
	0.22±0.08	0.18±0.08	0.20±0.10	0.05±0.05	-0.03±0.08	0.02±0.09	-0.04±0.08	0.14±0.07	0.06±0.06	0.14±0.10
HD 170053	0.18±0.11	0.11±0.12	0.21±0.07	0.01±0.11	-0.05±0.12	-0.08±0.13	-0.09±0.09	0.18±0.08	-0.05±0.10	0.32±0.10
	0.08±0.09	-0.01±0.12	0.18±0.07	-0.13±0.11	-0.06±0.08	-0.21±0.13	-0.22±0.09	0.13±0.08	-0.10±0.10	0.30±0.10
HD 170174	0.08±0.09	0.07±0.06	0.12±0.09	0.06±0.07	-0.04±0.13	-0.01±0.09	-0.05±0.06	0.03±0.08	-0.05±0.06	0.28±0.11
	0.16±0.07	0.15±0.05	0.16±0.09	0.13±0.06	-0.07±0.09	0.07±0.08	0.02±0.06	0.08±0.08	0.00±0.06	0.27±0.11
HD 170231	0.01±0.10	0.04±0.07	0.06±0.09	0.07±0.07	-0.04±0.12	0.01±0.09	-0.05±0.05	0.03±0.08	-0.06±0.05	0.38±0.11
	0.12±0.08	0.12±0.06	0.11±0.08	0.15±0.05	-0.08±0.09	0.10±0.08	0.04±0.05	0.10±0.08	0.00±0.05	0.36±0.11
α Boo	0.58±0.13	0.45±0.09	0.42±0.11	0.19±0.08	0.12±0.11	0.22±0.12	-0.02±0.09	0.31±0.08	0.04±0.07	-0.23±0.10
	0.60±0.08	0.47±0.08	0.42±0.11	0.22±0.07	0.12±0.08	0.24±0.12	0.00±0.09	0.32±0.08	0.05±0.07	-0.22±0.09
η Ser	0.09±0.11	0.12±0.08	0.09±0.08	0.08±0.05	0.00±0.13	-0.01±0.10	-0.05±0.06	0.10±0.08	0.00±0.06	0.08±0.14
	0.14±0.08	0.17±0.06	0.10±0.07	0.13±0.05	0.00±0.08	0.04±0.09	-0.01±0.05	0.12±0.08	0.02±0.06	0.07±0.09
ϵ Oph	0.04±0.10	0.05±0.08	0.11±0.09	0.03±0.06	-0.05±0.15	0.00±0.09	-0.02±0.09	0.05±0.08	-0.03±0.06	0.24±0.12
	0.05±0.08	0.06±0.08	0.11±0.07	0.05±0.05	-0.05±0.09	0.01±0.09	-0.01±0.08	0.06±0.08	-0.03±0.05	0.24±0.10
ξ Hya	-0.02±0.10	0.04±0.06	0.10±0.08	0.04±0.06	-0.08±0.12	-0.05±0.09	-0.04±0.05	0.06±0.08	-0.02±0.09	0.19±0.11
	0.03±0.08	0.08±0.05	0.12±0.07	0.08±0.06	-0.10±0.08	-0.01±0.09	0.00±0.05	0.08±0.08	0.00±0.09	0.18±0.09
β Aql	0.06±0.13	0.10±0.08	0.06±0.08	0.10±0.07	-0.03±0.11	-0.02±0.10	-0.05±0.06	0.04±0.08	0.01±0.05	0.08±0.15
	0.08±0.08	0.12±0.06	0.06±0.06	0.11±0.05	-0.04±0.08	0.00±0.09	-0.04±0.05	0.05±0.07	0.01±0.05	0.07±0.10

Notes. When available, the second row shows the results with the surface gravity fixed to the seismic value for each star. We use the usual notation $[X/Fe] = [\log \epsilon(X) - \log \epsilon(Fe)] - [\log \epsilon(X) - \log \epsilon(Fe)]_{\odot}$ with $\log \epsilon(X) = 12 + \log[N(X)/N(H)]$ (N is the number density of the species). The adopted solar abundances ($\log \epsilon_{\odot}$) are given in the first row (Grevesse & Sauval 1998).

Table A.5. Abundance data with $1-\sigma$ uncertainties for the mixing indicators.

	[Li/H]		[C/Fe]	[C/Fe] _{corr}	[N/Fe]	[O I 6300/Fe]	[O I 6300/Fe] _{corr}	[O triplet/Fe]	[Na/Fe]	[Na/Fe] _{corr}	¹² C/ ¹³ C
	LTE	NLTE	LTE	LTE	LTE	LTE	LTE	LTE	LTE	LTE	LTE
Sun	1.09	1.13	8.52	8.52	7.92	8.83	8.83	8.83	6.33	6.33	
HD 40726	+0.34±0.13	+0.43±0.13	-0.30	-0.28	0.45	-0.15	-0.12	...	0.25±0.05	0.26±0.05	...
HD 42911	<-1.15	<-0.99	-0.21	-0.16	0.36	-0.13	-0.07	...	0.18±0.08	0.20±0.08	...
HD 43023	<-1.40	<-1.29	-0.23	-0.25	0.39	-0.02	-0.04	...	0.10±0.06	0.09±0.06	...
HD 45398	-0.82±0.13	-0.50±0.13	-0.11	-0.17	0.16	-0.03	-0.10	...	0.24±0.14	0.22±0.14	...
HD 49429	<-1.00	<-0.90	-0.23	-0.25	0.32	-0.02	-0.05	...	0.12±0.06	0.11±0.06	...
HD 49566	-0.27±0.13	-0.18±0.13	-0.18	-0.20	0.38	-0.04	-0.06	...	0.14±0.06	0.13±0.06	...
	-0.25±0.12	-0.16±0.12	-0.15	-0.18	0.42	-0.05	-0.09	...	0.19±0.05	0.18±0.05	...
HD 50890	-0.07±0.16	+0.15±0.16	-0.40	-0.41	0.58	-0.24	-0.25	...	0.51±0.11	0.51±0.11	...
	-0.13±0.14	+0.09±0.14	-0.43	-0.41	0.57	-0.20	-0.17	...	0.41±0.11	0.42±0.11	...
HD 169370	-1.41±0.13	-1.19±0.13	-0.03	-0.14	0.06	0.08	-0.05	...	0.03±0.12	-0.01±0.12	...
	-1.41±0.12	-1.19±0.12	-0.04	-0.14	0.05	0.07	-0.06	...	0.02±0.10	-0.01±0.10	...
HD 169751	-0.52±0.13	-0.38±0.13	-0.26	-0.26	0.29	-0.10	-0.10	...	0.08±0.09	0.08±0.09	...
	-0.50±0.12	-0.36±0.12	-0.25	-0.26	0.31	-0.10	-0.11	...	0.11±0.08	0.11±0.08	...
HD 170008	<-0.90	<-0.83	-0.03	-0.17	0.02	0.03	-0.14	...	0.03±0.07	-0.02±0.07	...
	<-0.90	<-0.83	-0.03	-0.16	0.01	0.03	-0.14	...	0.02±0.07	-0.02±0.07	...
HD 170031	-1.39±0.13	-1.15±0.13	-0.11	-0.11	0.24	-0.03	-0.03	...	0.17±0.15	0.17±0.15	...
	-1.42±0.12	-1.18±0.12	-0.13	-0.11	0.20	-0.05	-0.03	...	0.11±0.12	0.12±0.12	...
HD 171427	-0.38±0.13	-0.20±0.13	-0.22	-0.23	0.59	-0.06	-0.07	...	0.33±0.05	0.33±0.05	...
HD 175294	<-1.20	<-1.03	-0.25	-0.15	0.43	-0.12	0.00	0.14±0.26	0.26±0.08	0.29±0.08	16±2
HD 175679	+0.15±0.13	+0.26±0.13	-0.24	-0.20	0.46	-0.05	0.00	0.05±0.15	0.17±0.05	0.18±0.05	17±5
	+0.20±0.12	+0.31±0.12	-0.19	-0.18	0.56	-0.09	-0.08	-0.02±0.14	0.29±0.05	0.29±0.05	17±5
HD 178484	-0.90±0.13	-0.65±0.13	0.00	-0.12	0.17	0.08	-0.08	...	0.23±0.10	0.19±0.10	...
	-0.92±0.12	-0.67±0.12	-0.02	-0.13	0.17	0.07	-0.07	...	0.19±0.10	0.15±0.10	...
HD 181907	<-1.30	<-1.11	-0.14	-0.18	0.26	0.05	0.00	0.29±0.27	0.12±0.09	0.11±0.09	9±1
	<-1.25	<-1.06	-0.13	-0.19	0.28	0.05	-0.02	0.25±0.23	0.17±0.05	0.15±0.05	9±1
HD 170053	+0.11±0.13	+0.36±0.13	-0.15	-0.20	0.42	-0.04	-0.11	...	0.27±0.13	0.25±0.13	...
	+0.06±0.12	+0.31±0.12	-0.18	-0.19	0.43	-0.06	-0.07	...	0.13±0.13	0.13±0.13	...
HD 170174	-0.48±0.13	-0.36±0.13	-0.20	-0.20	0.46	-0.03	-0.03	...	0.20±0.06	0.20±0.06	...
	-0.45±0.12	-0.33±0.12	-0.17	-0.20	0.52	-0.05	-0.08	...	0.28±0.06	0.27±0.06	...
HD 170231	+0.24±0.13	+0.34±0.13	-0.27	-0.25	0.46	-0.09	-0.07	...	0.16±0.07	0.17±0.07	...
	+0.26±0.12	+0.36±0.12	-0.23	-0.24	0.54	-0.12	-0.13	...	0.25±0.06	0.25±0.06	...
α Boo	<-2.50	<-2.24	0.18	-0.21	0.22	0.43	-0.02	0.69±0.20	0.19±0.10	0.07±0.10	8±1
	<-2.45	<-2.19	0.19	-0.21	0.22	0.44	-0.02	0.68±0.20	0.21±0.09	0.09±0.09	8±1
η Ser	<-2.00	<-1.88	-0.08	-0.16	0.25	0.06	-0.04	...	0.05±0.09	0.02±0.09	...
	<-1.90	<-1.78	-0.07	-0.16	0.28	0.06	-0.06	...	0.10±0.08	0.07±0.08	...
ϵ Oph	<-0.80	<-0.66	-0.27	-0.28	0.30	-0.08	-0.09	...	0.09±0.06	0.09±0.06	...
	<-0.80	<-0.66	-0.26	-0.28	0.31	-0.08	-0.10	...	0.10±0.05	0.09±0.05	...
ξ Hya	+0.07±0.13	+0.19±0.13	-0.25	-0.20	0.43	-0.14	-0.07	...	0.24±0.08	0.26±0.08	...
	+0.09±0.12	+0.21±0.12	-0.24	-0.20	0.47	-0.15	-0.10	...	0.28±0.07	0.29±0.07	...
β Aql	<-1.20	<-1.12	0.02	-0.06	-0.13	0.01	-0.09	...	0.03±0.09	0.00±0.09	...
	<-1.15	<-1.07	0.02	-0.07	-0.12	0.00	-0.11	...	0.04±0.06	0.01±0.06	...

Notes. When available, the second row shows the results with the surface gravity fixed to the seismic value for each star. We use the usual notation $[X/Fe] = [\log \epsilon(X) - \log \epsilon(Fe)] - [\log \epsilon(X) - \log \epsilon(Fe)]_{\odot}$ with $\log \epsilon(X) = 12 + \log[N(X)/N(H)]$ (N is the number density of the species). The adopted solar abundances ($\log \epsilon_{\odot}$) are given in the first row and are taken from Grevesse & Sauval (1998), except for Li for which we adopt $\log \epsilon(Li)_{\odot} = 1.09$ and 1.13 in LTE and NLTE, respectively (Sect. 5.2.1). For lithium, the following notation is used: $[Li/H] = \log N(Li) - \log N(Li)_{\odot}$. Lithium abundances corrected for departures from LTE (Lind et al. 2009) are also provided. The values with the “corr” subscript were corrected for the chemical evolution of the Galaxy (Sect. 9). The $1-\sigma$ uncertainties for the C, N, and the O abundances derived from [O I] $\lambda 6300$ are 0.09, 0.13, and 0.14 dex, respectively. With the gravity fixed to the seismic value, this translates to 0.09, 0.13, and 0.10 dex. Due to the difficulty in fitting the CNO features in HD 50890, the uncertainties for the C, N, and O abundances are 0.12, 0.14, and 0.16 dex (0.12, 0.14, and 0.12 dex for the gravity fixed to the seismic value).

Table A.6. Logarithmic abundance ratios of C, N, and O.

	[N/C]	[N/C] _{corr}	[N/O]	[N/O] _{corr}	[C/O]	[C/O] _{corr}
HD 40726	0.75	0.73	0.60	0.57	-0.15	-0.16
HD 42911	0.57	0.52	0.49	0.43	-0.08	-0.09
HD 43023	0.62	0.64	0.41	0.43	-0.21	-0.20
HD 45398	0.27	0.33	0.19	0.26	-0.08	-0.06
HD 49429	0.55	0.57	0.34	0.37	-0.21	-0.20
HD 49566	0.56	0.58	0.42	0.44	-0.14	-0.14
	0.57	0.60	0.47	0.51	-0.10	-0.09
HD 50890	0.98	0.99	0.82	0.83	-0.16	-0.16
	1.00	0.98	0.77	0.74	-0.23	-0.24
HD 169370	0.09	0.20	-0.02	0.11	-0.11	-0.08
	0.09	0.19	-0.02	0.11	-0.11	-0.08
HD 169751	0.55	0.55	0.39	0.39	-0.16	-0.16
	0.56	0.57	0.41	0.42	-0.15	-0.15
HD 170008	0.05	0.19	-0.01	0.16	-0.06	-0.02
	0.04	0.17	-0.02	0.15	-0.06	-0.02
HD 170031	0.35	0.35	0.27	0.27	-0.08	-0.08
	0.33	0.31	0.25	0.23	-0.08	-0.08
HD 171427	0.81	0.82	0.65	0.66	-0.16	-0.16
HD 175294	0.68	0.58	0.55	0.42	-0.13	-0.16
HD 175679	0.70	0.66	0.51	0.45	-0.19	-0.20
	0.75	0.74	0.65	0.64	-0.10	-0.10
HD 178484	0.17	0.29	0.09	0.25	-0.08	-0.04
	0.19	0.30	0.10	0.24	-0.09	-0.06
HD 181907	0.40	0.44	0.21	0.26	-0.19	-0.18
	0.41	0.47	0.23	0.30	-0.18	-0.16
HD 170053	0.57	0.62	0.46	0.53	-0.11	-0.09
	0.61	0.62	0.49	0.50	-0.12	-0.12
HD 170174	0.66	0.66	0.49	0.49	-0.17	-0.17
	0.69	0.72	0.57	0.60	-0.12	-0.11
HD 170231	0.73	0.71	0.55	0.53	-0.18	-0.18
	0.77	0.78	0.66	0.67	-0.11	-0.11
α Boo	0.04	0.43	-0.21	0.24	-0.25	-0.19
	0.03	0.43	-0.22	0.24	-0.25	-0.18
η Ser	0.33	0.41	0.19	0.29	-0.14	-0.12
	0.35	0.44	0.22	0.34	-0.13	-0.10
ϵ Oph	0.57	0.58	0.38	0.39	-0.19	-0.19
	0.57	0.59	0.39	0.41	-0.18	-0.18
ξ Hya	0.68	0.63	0.57	0.50	-0.11	-0.12
	0.71	0.67	0.62	0.57	-0.09	-0.10
β Aql	-0.15	-0.07	-0.14	-0.03	0.01	0.03
	-0.14	-0.05	-0.12	-0.01	0.02	0.04

Notes. When available, the second row shows the results with the surface gravity fixed to the seismic value for each star. The values with the “corr” subscript were corrected for the chemical evolution of the Galaxy (Sect. 9). The $1\text{-}\sigma$ uncertainties for [N/C], [N/O], and [C/O] are 0.10, 0.15, and 0.12 dex, respectively. With the surface gravity fixed to the seismic value, this translates to 0.08, 0.13, and 0.09 dex. Due to the difficulty in fitting the CNO features in HD 50890, the uncertainties for [N/C], [N/O], and [C/O] are 0.13, 0.17, and 0.14 dex (0.11, 0.15, and 0.12 dex for the gravity fixed to the seismic value).